

Geomagnetic semblance and dipolar–multipolar transition in top-heavy double-diffusive geodynamo models

Théo Tassin , Thomas Gastine  and Alexandre Fournier 

Université de Paris, Institut de Physique du Globe de Paris, CNRS, F-75005 Paris, France. E-mail: tassin@ipgp.fr

Accepted 2021 April 12. Received 2021 April 1; in original form 2020 December 18

SUMMARY

Convection in the liquid outer core of the Earth is driven by thermal and chemical perturbations. The main purpose of this study is to examine the impact of double-diffusive convection on magnetic field generation by means of 3-D global geodynamo models, in the so-called ‘top-heavy’ regime of double-diffusive convection, when both thermal and compositional background gradients are destabilizing. Using a linear eigensolver, we begin by confirming that, compared to the standard single-diffusive configuration, the onset of convection is facilitated by the addition of a second buoyancy source. We next carry out a systematic parameter survey by performing 79 numerical dynamo simulations. We show that a good agreement between simulated magnetic fields and the geomagnetic field can be attained for any partitioning of the convective input power between its thermal and chemical components. On the contrary, the transition between dipole-dominated and multipolar dynamos is found to strongly depend on the nature of the buoyancy forcing. Classical parameters expected to govern this transition, such as the local Rossby number—a proxy of the ratio of inertial to Coriolis forces—or the degree of equatorial symmetry of the flow, fail to capture the dipole breakdown. A scale-dependent analysis of the force balance instead reveals that the transition occurs when the ratio of inertial to Lorentz forces at the dominant length scale reaches 0.5, regardless of the partitioning of the buoyancy power. The ratio of integrated kinetic to magnetic energy E_k/E_m provides a reasonable proxy of this force ratio. Given that $E_k/E_m \approx 10^{-4} - 10^{-3}$ in the Earth’s core, the geodynamo is expected to operate far from the dipole–multipole transition. It hence appears that the occurrence of geomagnetic reversals is unlikely related to dramatic and punctual changes of the amplitude of inertial forces in the Earth’s core, and that another mechanism must be sought.

Key words: Composition and structure of the core; Core; Dynamo: theories and simulations; Magnetic field variations through time; Numerical modelling.

1 INTRODUCTION

The exact composition of Earth’s core remains unclear but it is admitted that it is mainly composed of iron and nickel with a mixture of lighter elements in liquid state, such as silicon or oxygen (see Hirose *et al.* 2013, for a review). The ongoing crystallization of the inner core releases light elements and latent heat at the inner-core boundary (ICB), while the mantle extracts thermal energy from the outer core at the core–mantle boundary (CMB). This combination of processes is responsible for the joint presence of thermal and chemical inhomogeneities within the outer core.

Convection with two distinct sources of mass anomaly is termed *double-diffusive* convection (e.g. Radko 2013). A key physical parameter of double-diffusive convection is the Lewis number Le , defined as the ratio of the thermal diffusivity κ_T to the chemical diffusivity κ_ξ . In the liquid core of terrestrial planets, Le reaches at least $10 - 10^4$ (e.g. Loper & Roberts 1981; Li *et al.* 2000).

Under double-diffusive conditions, the increase of the background density with depth does not necessarily imply the stability of the fluid in response to perturbations. As shown in Fig. 1, three configurations can be considered:

- (i) The *salt fingering* regime, when the background thermal gradient ∇T_0 is stabilizing and the mean compositional gradient $\nabla \xi_0$ is destabilizing.
- (ii) The *semi-convection* regime, when ∇T_0 is destabilizing and $\nabla \xi_0$ is stabilizing.
- (iii) The *top-heavy convection* regime (also known as double-buoyant), when both ∇T_0 and $\nabla \xi_0$ are destabilizing.

These three cases correspond to three quadrants in Fig. 1, which is inspired by Ruddick (1983). Note that being located inside one of these three quadrants does not necessarily guarantee that convection occurs, since, for all configurations, the onset does not coincide with the origin of the diagram: a critical contrast in temperature,

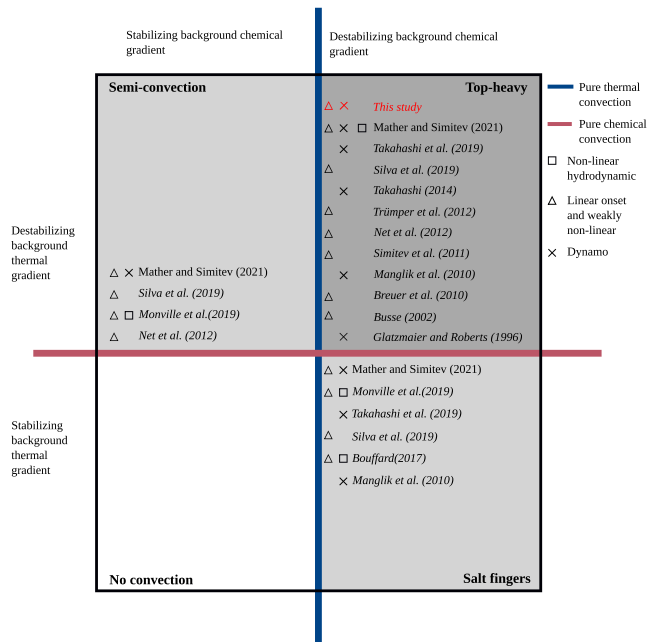


Figure 1. Schematic overview of previous studies on double-diffusive convection and dynamo action in terrestrial interiors, inspired by the regime diagram of Ruddick (1983). The parameter space has two independent directions, defined by the prescribed background temperature and composition gradients, respectively. It is divided into four quadrants, since each gradient can have a stabilizing or destabilizing effect on fluid motion. The vertical and horizontal lines correspond to purely thermal and purely chemical convection, respectively (in which case there exists a unique destabilizing background profile). The publications that appear in the three quadrants of dynamic interest are the following: Glatzmaier & Roberts (1996), Busse (2002), Breuer *et al.* (2010), Manglik *et al.* (2010), Simitev (2011), Net *et al.* (2012), Trümper *et al.* (2012), Takahashi (2014), Bouffard (2017), Monville *et al.* (2019), Silva *et al.* (2019), Takahashi *et al.* (2019) and Mather & Simitev (2021). Crosses denote dynamo studies, triangles linear and weakly non-linear hydrodynamic studies and squares non-linear hydrodynamic studies.

or composition or both, is required to trigger convective motions. In addition, this diagram does not account for the influence of background rotation (see Monville *et al.* 2019, for the impact of rotation on the onset in the salt fingers regime), or a magnetic field, on the onset.

Double-diffusive convection has been extensively studied in physical oceanography (e.g. Radko 2013), as heat and salinity provide two different sources of buoyancy for seawater, as well as in stellar interiors (e.g. Spiegel 1972), where the molecular diffusivity of composition is only a tiny fraction of the diffusivity of temperature (e.g. Moll *et al.* 2016, and references therein). To our knowledge, a limited number of studies have been devoted to the analysis of double-diffusive convection in the context of Earth’s core, or more generally in the context of the metallic core of terrestrial planets. They are listed in Fig. 1, with possibly several occurrences of a given study when several of the aforementioned regimes were considered. It appears that the top-heavy configuration has been investigated the most; this is also the configuration we shall focus on in this work.

Previous studies devoted to the top-heavy regime are listed in the top-right quadrant of Fig. 1, starting with hydrodynamic, non-magnetic studies. Considering the $Le \gg 1$ limit for a fluid filling a rapidly rotating annulus, Busse (2002) theoretically predicted that

the addition of chemical buoyancy facilitated the onset of standard thermal convection, in two ways. First by lowering the critical value of the Rayleigh number required to trigger the classical spiralling thermal Rossby waves of size and frequency proportional to $E^{1/3}$ and $E^{-2/3}$, respectively, where $E = \nu/\Omega D^2$ is the non-dimensional Ekman number, ν being the kinematic viscosity, Ω the rotation rate and D the size of the fluid domain. Secondly, and more importantly, by enabling a second class of instability. The latter is characterized by a much lower onset, independent of E , a critical length scale of the order of the size of the fluid domain, and a very small frequency, proportional to E . Busse (2002) referred to this class of instability as ‘nearly steady’ (i.e. slow) convection, and he argued that it could facilitate ‘immensely’ convection in Earth’s core, though with several caveats (see Busse 2002, for details). Simitev (2011) pushed the analysis further for various Le , and stressed that the critical onset curve for convective instability in a rotating annulus forms disconnected regions of instabilities in the parameter space. In particular, the second family of modes (i.e. the slow modes) are stable whenever the compositional gradient is destabilizing. Trümper *et al.* (2012), Net *et al.* (2012) and Silva *et al.* (2019) studied the onset of double-diffusive convection in a spherical shell geometry. In the top-heavy regime with $3 \leq Le \leq 10$, Trümper *et al.* (2012) confirmed that the addition of a secondary buoyancy source facilitates the convective onset. Net *et al.* (2012) showed that the properties of the critical onset mode, such as its drift frequency or its azimuthal wave number, strongly depends on the fractioning between thermal and compositional buoyancy. Using a linear eigensolver, Silva *et al.* (2019) carried out a systematic survey of the onset of convection in spherical shells for the different double-diffusive regimes. In the top-heavy configuration with $Le = 25$, they showed that the convection onset is characterized by an abrupt change between the purely thermal and the purely compositional eigenmodes depending on the relative proportion of the two buoyancy sources. In addition, they demonstrated that the onset mode features the same asymptotic dependence on the Ekman number as classical thermal Rossby waves over the entire top-heavy regime (top-right quadrant of Fig. 1), thereby casting some doubt on the likelihood of the occurrence of slow modes.

Trümper *et al.* (2012) performed a series of non-linear, moderately supercritical, rotating convection calculations at constant $Le = 10$, for different proportions of chemical and thermal driving. To that end, they conducted a parameter survey, varying the chemical and thermal Rayleigh numbers, to be defined below, while keeping their sum constant. This way of sampling the parameter space, however, does not guarantee that the total buoyancy input power stays constant. This complicates the interpretation of their results, for instance regarding the influence of compositional and thermal forcings on the convective flow properties.

Let us now turn our attention to the few self-consistent dynamo calculations in the top-heavy regime published to date (marked with a cross in the top-right quadrant of Fig. 1). The first integration was reported by Glatzmaier & Roberts (1996). This calculation was an anelastic, double-diffusive extension of the celebrated Boussinesq simulation of the geodynamo by Glatzmaier & Roberts (1995). Glatzmaier & Roberts (1996) assumed enhanced and equal values of the diffusivities, that is $Le = 1$. Consequently, that simulation did not exhibit stark differences with the purely thermal convective model, except that the dipole did not reverse over the course of the simulated 40 000 yr. The second numerical investigation of geodynamo models driven by top-heavy convection was conducted by Takahashi (2014). His models were based on the Boussinesq approximation with $Le = 10$ and relatively large Ekman numbers

($E \geq 2 \times 10^{-4}$). In addition, Mather & Simitev (2021) identified a few top-heavy Boussinesq dynamos with $Le = 25$ and $E = 10^{-4}$, that used stress-free mechanical boundary conditions and appeared to be close to onset. Top-heavy dynamo simulations were also performed by Manglik *et al.* (2010) and Takahashi *et al.* (2019) in the context of modelling Mercury's dynamo.

Double-diffusive models of the geodynamo are the exception rather than the rule, essentially on the account of Occam's razor. Efforts carried out in the community since the mid-1990s have been towards understanding the most salient properties of the geomagnetic field using a minimum number of ingredients (e.g. Wicht & Sanchez 2019, for a review). To that end, the *codensity* formalism introduced by Braginsky & Roberts (1995) is particularly attractive: it assumes that the molecular values of κ_{ξ} and κ_T can be replaced by a single turbulent transport property. Consequently, the mass anomaly field can be described by a single scalar, termed the codensity, that aggregates the two sources of mass anomaly. This approach has the benefit of (i) removing one degree of freedom and (ii) mitigating the numerical cost by suppressing the scale separation between chemical and thermal fields when $Le \gg 1$. With regard to Fig. 1, this amounts to restricting the diagram to either the vertical or the horizontal line.

The codensity formalism was quite successful in reproducing some of the best constrained features of the geomagnetic field and its secular variation (e.g. Christensen *et al.* 2010; Aubert *et al.* 2013; Schaeffer *et al.* 2017; Wicht & Sanchez 2019). Most geodynamo models actually assume that the diffusivity of the codensity field equals the kinematic viscosity, yielding a Prandtl number of unity. A remarkable property of the geodynamo that remains to be explained satisfactorily from the numerical modelling standpoint, is its ability to reverse its polarity every once in a while, that is to go from a dipole-dominated state to another dipole-dominated state through a transient multipolar state (see e.g. Valet & Fournier 2016, for a recent review of the relevant palaeomagnetic data). A possibility is that the geodynamo has been, at least punctually in its history, in a dynamic state that can enable the switch between dipole-dominated and multipolar states to occur. A key question that follows is therefore: what are the physical processes that control the transition between dipole-dominated dynamos and multipolar dynamos? This has been analysed intensively numerically, starting with the systematic approach of Kutzner & Christensen (2002), who demonstrated that a stronger convective driving led to a dipole breakdown, and that for intermediate values of the forcing, the simulated field could oscillate between dipolar and multipolar states.

Sreenivasan & Jones (2006) showed that an increasing role of inertia (through stronger driving) perturbed the dominant Magneto–Archimedean–Coriolis force balance to the point that it led to a less structured and less dipole-dominated magnetic field. In the same vein, Christensen & Aubert (2006) assumed that the transition is due to a competition between inertia and Coriolis force. They introduced a diagnostic quantity termed the *local Rossby number* $Ro_L = u_{\text{rms}}/\Omega L$, as a proxy of this force ratio. Here u_{rms} denotes the average flow speed and L is an integral measure of the convective flow scale. Based on their ensemble of simulations, Christensen & Aubert (2006) concluded that the breakdown of the dipole occurred above a critical value of about $Ro_L \simeq 0.12$, in what appeared a relatively sharp transition (see also Christensen 2010). If this reasoning gives a satisfactory account of the numerical data set, its extrapolation to Earth's core regime raises questions (e.g. Oruba & Dormy 2014). Since the geomagnetic dipole reversed in the past, the numerical evidence collected so far (see Wicht & Tilgner 2010,

for a review) suggests that the geodynamo could lie close to the transition between dipolar and multipolar states. This implies that Ro_L could be of the order of 0.1 for the Earth's core. Geomagnetic reversals should then reflect the action of a convective feature of scale L of about 50 m (see Davidson 2013; Aubert *et al.* 2017). It is very unlikely that such a small-scale flow could significantly alter a dipole-dominated magnetic field.

According to Soderlund *et al.* (2012), the breakdown of the dipole is rather due to a decrease of the relative helicity of the flow. In numerical dynamo simulations, coherent helicity favours large-scale poloidal magnetic field through the α -effect (see Parker 1955) at work in convection columns and it therefore contributes actively to the production and the maintenance of dipolar field (e.g. Olson *et al.* 1999). Conversely, the dipolar field can promote a more helical flow, with the Lorentz force enhancing the flow along the axis of convection columns, as shown by Sreenivasan & Jones (2011). By measuring the integral force balance for dipolar and multipolar numerical dynamos, Soderlund *et al.* (2012) noted that the Coriolis force remained dominant, even in multipolar models. Accordingly, they suggested that, in their models, the modification of the flow structure was rather controlled by a competition of second-order forces, with the ratio of inertia to viscous forces as the parameter controlling the transition.

The role played by viscous effects was further stressed by Oruba & Dormy (2014), who proposed that the transition from dipolar to multipolar dynamos in the numerical data set was controlled by a triple force balance between Coriolis force, viscosity and inertia. A local Rossby number constructed using the viscous lengthscale, $E^{1/3} \mathcal{D}$, as opposed to the integral scale L discussed above, carries the same predictive power in separating dipolar from multipolar dynamo models (their Fig. 4). This argument was subsequently refined by Garcia *et al.* (2017), who included the Prandtl number dependence of the critical convective length scale when defining the local Rossby number. From a mechanistic point of view, Garcia *et al.* (2017) showed that the dipole breakdown was not necessarily correlated to a decrease of the relative helicity, but rather to a weakening of the equatorial symmetry of the flow. Introducing the proportion of kinetic energy contained in this equatorially symmetric component, they demonstrated that the transition could be satisfactorily explained by a sharp decrease of that quantity when the refined local Rossby number exceeded a value of 0.2 (their fig. 3d). This would imply that the transition from a dipolar state to a multipolar state would essentially be a hydrodynamic transition. Discussing the implication of their results for the geodynamo, they clearly stated that the role of inertia was presumably overestimated in the numerical data set that had been investigated so far, stressing the need for stronger field dynamos, where the magnetic field could possibly have an active role.

The early numerical data set admittedly contained a majority of dynamos operating at large Ekman numbers, and relatively low magnetic Prandtl number Pm . In the dynamos studied by Soderlund *et al.* (2012), the convective flow was not dramatically altered by the presence of a self-sustained magnetic field. Since then, a large number of simulations have been published with lower values of E and comparatively larger values of Pm (Yadav *et al.* 2016; Schaeffer *et al.* 2017; Schwaiger *et al.* 2019; Menu *et al.* 2020). For those strong-field dynamos, in the sense of a ratio of bulk magnetic energy to bulk kinetic energy larger than one, the magnetic field has a significant impact on the flow, and on the dipolar–multipolar transition. Menu *et al.* (2020) reported simulations with a prevailing Lorentz force, that remain dipolar way beyond the supposedly critical $Ro_L \simeq 0.12$ value. Given that Earth hosts a strong-field dynamo, it is

then worth investigating whether the competition between Lorentz force and inertia may actually lead to the transition.

In order to shed light on this particular issue, and to further strengthen our understanding of double-diffusive dynamos, we have performed a suite of 79 novel dynamo models, comprising 44, 20, 15 simulations with top-heavy, purely thermal, purely chemical driving, respectively. The goal of this work is twofold: on the one hand, we will follow an approach similar to that of Takahashi (2014) and study to which extent the relative proportion of chemical to thermal driving impacts the earth-likeness (in a morphological sense) of the simulated magnetic fields. On the other hand, we will examine whether this proportion has an impact on the dipolar to multipolar transition. Takahashi (2014) reported a drop of the dipolarity when the relative contribution of thermal convection to the total input power exceeds 65 per cent. We will analyse whether this was a fortuitous consequence of the cases he considered, and whether we can find a more general rationale to explain the transition, by careful inspection of the force balance at work.

This paper is organized as follows: the derivation of the governing equations and their numerical approximations are presented in Section 2. The results are described in Section 3. We proceed by firstly investigating the onset of convection for top-heavy convection. The impact of the input power distribution on the Earth-likeness is then explored. Finally we examine the transition between dipolar and multipolar dynamos. Section 4 discusses the results and their geophysical implications.

2 MODEL AND METHODS

2.1 Hypotheses

We operate in spherical coordinates (r, θ, φ) and consider a spherical shell of volume V_o filled with a fluid delimited by the ICB, located at the radius r_i , on one side and by the CMB, located at the radius r_o , on the other side with $r_i/r_o = 0.35$. The shell rotates about the $\hat{\mathbf{z}}$ -axis with a constant rotation rate Ω , where $\hat{\mathbf{z}}$ is the unit vector in the direction of rotation. The equation of state

$$\rho = \rho_0[1 - \alpha_T(T - T_0) - \alpha_\xi(\xi - \xi_0)], \quad (1)$$

describes how the density of the fluid ρ varies with temperature T and composition ξ . In this equation, α_T and α_ξ are the coefficients of thermal and chemical expansion, T_0 , ρ_0 and ξ_0 the average temperature, density and composition of lighter elements in the outer core.

The properties of the fluid, including its kinematic viscosity ν , its magnetic diffusivity η , its specific heat C_p , its chemical and thermal diffusivity (κ_ξ, κ_T), its coefficients of thermal and chemical expansion (α_T, α_ξ) are assumed to be spatially uniform and constant in time. Due to the almost uniform density in the outer core, we also assume a linear variation of the acceleration of gravity \mathbf{g} with radius. The physical and thermodynamic properties of the Earth's core relevant for this study are given in Table 1.

2.2 Governing equations

Convection of an electrically conducting fluid gives rise to a magnetic field \mathbf{B} . The state of the fluid is then described by the velocity field \mathbf{u} , the magnetic field \mathbf{B} , the pressure p , the temperature T and the composition ξ . The equations governing the dynamics of the flow under the Boussinesq approximation are cast in a non-dimensional form. We adopt the thickness of the shell $\mathcal{D} = r_o - r_i$

as reference length scale and the viscous diffusion time \mathcal{D}^2/ν as timescale. A velocity scale is then given by ν/\mathcal{D} . Composition is scaled by $\partial\xi = |\partial_r \xi(r_i)|\mathcal{D}$, pressure by $\rho_0(\nu/\mathcal{D})^2$, power by $\nu^3 \rho_0/\mathcal{D}$ and magnetic induction by $\sqrt{\rho_0 \mu_0 \eta \Omega}$, where μ_0 is the magnetic permeability of vacuum. Temperature unit is based on the temperature gradient at r_i , $\partial T = |\partial_r T(r_i)|\mathcal{D}$, or at r_o , $\partial T = |\partial_r T(r_o)|\mathcal{D}$, depending on the thermal boundary conditions. Under the Boussinesq approximation, the equation for the conservation of mass is

$$\nabla \cdot \mathbf{u} = 0. \quad (2)$$

The dynamics of the flow is described by the Navier–Stokes equation, expressed in the frame rotating with the mantle

$$\partial_t \mathbf{u} + \mathbf{u} \cdot \nabla \mathbf{u} = -\frac{2}{E} \hat{\mathbf{z}} \times \mathbf{u} + \left(\frac{Ra_T}{Pr} T + \frac{Ra_\xi}{Sc} \xi \right) \frac{r}{r_o} \hat{\mathbf{r}} - \nabla p + \frac{1}{E Pm} [(\nabla \times \mathbf{B}) \times \mathbf{B}] + \nabla^2 \mathbf{u}, \quad (3)$$

where $\hat{\mathbf{r}}$ is the unit vector in the radial direction. The time evolution of the magnetic field under the magnetohydrodynamics approximation is given by the induction equation

$$\partial_t \mathbf{B} = \nabla \times (\mathbf{u} \times \mathbf{B}) + \frac{1}{Pm} \nabla^2 \mathbf{B} \quad \text{with} \quad \nabla \cdot \mathbf{B} = 0. \quad (4)$$

Finally, the evolution of entropy and composition are governed by the similar transport equations

$$\partial_t T + \mathbf{u} \cdot \nabla T = \frac{1}{Pr} \nabla^2 T + h^T, \quad (5)$$

and

$$\partial_t \xi + \mathbf{u} \cdot \nabla \xi = \frac{1}{Sc} \nabla^2 \xi + h^\xi, \quad (6)$$

where h^T is a volumetric internal heating and h^ξ a chemical volumetric source.

The set of eqs (2)–(6) is governed by 6 dimensionless numbers: The Ekman number E expresses the ratio between viscous and Coriolis forces

$$E = \frac{\nu}{\Omega \mathcal{D}^2},$$

the Prandtl (Schmidt) number between viscous and thermal (chemical) diffusivities

$$Pr = \frac{\nu}{\kappa_T} \quad \text{and} \quad Sc = \frac{\nu}{\kappa_\xi}$$

and the magnetic Prandtl number between viscous and magnetic diffusivities

$$Pm = \frac{\nu}{\eta}.$$

The thermal and chemical Rayleigh numbers

$$Ra_T = \frac{\alpha_T g_o \mathcal{D}^3 \partial T}{\nu \kappa_T} \quad \text{and} \quad Ra_\xi = \frac{\alpha_\xi g_o \mathcal{D}^3 \partial \xi}{\nu \kappa_\xi},$$

where g_o is the gravitational acceleration at the CMB, measure the vigour of thermal and chemical convection. Note that the Lewis number Le discussed in the Introduction is the ratio of the Schmidt number to the Prandtl number,

$$Le = \frac{\kappa_T}{\kappa_\xi} = \frac{Sc}{Pr}.$$

Table 2 provides estimates of these control parameters for the Earth's core. These non-dimensional number express the ratio of characteristic physical timescales

$$E = \frac{\tau_\Omega}{\tau_\nu}, \quad Pm = \frac{\tau_\eta}{\tau_\nu} \quad \text{and} \quad Le = \frac{\tau_\xi}{\tau_T},$$

Table 1. Physical and thermodynamic parameters of Earth’s outer core relevant for this study. The corresponding references are listed in the rightmost column, which may comprise several entries if a bracket of values is provided.

Definition	Symbol	Value	Reference (lower bound–upper bound)
Inner radius	r_i	1221.5 km	Dziewonski & Anderson (1981)
Outer radius	r_o	3480 km	Dziewonski & Anderson (1981)
Earth angular velocity	Ω	$7.29 \times 10^{-5} \text{ rad} \cdot \text{s}^{-1}$	
Gravitational acceleration at CMB	g_o	$10.68 \text{ m} \cdot \text{s}^{-2}$	Dziewonski & Anderson (1981)
Core density at CMB	ρ_o	$9 \times 10^3 \text{ kg} \cdot \text{m}^{-3}$	Dziewonski & Anderson (1981)
Specific heat	C_p	$(850 \pm 80) \text{ J} \cdot \text{kg}^{-1} \cdot \text{K}^{-1}$	Labrosse (2003)
Heating power from core	Q	6 – 16 TW	Buffett (2015)
Thermal conductivity at CMB	k_T	$25 - 100 \text{ W} \cdot \text{m}^{-1} \cdot \text{K}^{-1}$	Konôpková <i>et al.</i> (2016), Pozzo <i>et al.</i> (2013), Zhang <i>et al.</i> (2020)
Thermal diffusivity	κ_T	$(0.3 - 1.4) \times 10^{-5} \text{ m}^2 \cdot \text{s}^{-1}$	Estimated using values of k_T , ρ_o and C_p .
Coefficient of thermal expansion	α_T	$(1.3 \pm 0.1) \times 10^{-5} \text{ K}^{-1}$	Labrosse (2003)
Kinematic viscosity	ν	$10^{-6} \text{ m}^2 \cdot \text{s}^{-1}$	Roberts & King (2013)
Magnetic diffusivity	η	$0.5 - 2.9 \text{ m}^2 \cdot \text{s}^{-1}$	Pozzo <i>et al.</i> (2013), Konôpková <i>et al.</i> (2016)
Estimated magnetic field strength	B_{rms}	$4 \times 10^{-3} \text{ T}$	Gillet <i>et al.</i> (2010)
Superadiabatic composition contrast	$\Delta\xi$	0.02 - 0.053	Badro <i>et al.</i> (2007), Anufriev <i>et al.</i> (2005)
Chemical diffusivity	κ_ξ	$(3 \times 10^{-9} - 4.2 \times 10^{-7}) \text{ m}^2 \cdot \text{s}^{-1}$	Loper & Roberts (1981), Li <i>et al.</i> (2000)
Coefficient of chemical expansion	α_ξ	0.6 – 0.83	Braginsky & Roberts (1995), Labrosse (2015)
Estimated flow velocity	u_{rms}	$(0.3 - 2.0) \times 10^{-3} \text{ m} \cdot \text{s}^{-1}$	Finlay & Amit (2011)

Table 2. Dimensionless control parameters. The two rightmost columns provide estimates of these parameters for Earth’s core and the values spanned by the simulations computed in this study. Earth’s core values were estimated thanks to Table 1.

Name	Symbol	Definition	Core	This study
Ekman	E	$\nu/\Omega\mathcal{D}^2$	10^{-15}	$10^{-5}-10^{-4}$
Thermal Rayleigh	Ra_T	$\alpha_T g_o \mathcal{D}^3 \partial T / \nu \kappa_T$	$10^{26}-10^{28}$	10^6-10^{10}
Chemical Rayleigh	Ra_ξ	$\alpha_\xi g_o \mathcal{D}^3 \partial \xi / \nu \kappa_\xi$	$10^{30}-10^{33}$	10^7-10^{12}
Magnetic Prandtl	Pm	ν/η	$(3.4-20) \times 10^{-7}$	0.5–5
Thermal Prandtl	Pr	ν/κ_T	0.08–0.25	0.3
Schmidt	Sc	ν/κ_ξ	2–300	3
Lewis	Le	κ_T/κ_ξ	9–4000	10

Table 3. Characteristic timescales for the Earth’s core. The values were estimated thanks to Table 1.

Name	Symbol	Definition	Core
Typical rotation time	τ_Ω	$1/\Omega$	4 hr
Turnover time	τ_{adv}	$\mathcal{D}/u_{\text{rms}}$	30–250 yr
Magnetic diffusion time	τ_η	\mathcal{D}^2/η	10^5-10^6 yr
Thermal diffusion time	τ_T	\mathcal{D}^2/κ_T	10^9-10^{10} yr
Viscous diffusion time	τ_ν	\mathcal{D}^2/ν	10^{11} yr
Chemical diffusion time	τ_ξ	\mathcal{D}^2/κ_ξ	$10^{11}-10^{13}$ yr

where $\tau_\Omega = 1/\Omega$ is the typical rotation time, $\tau_\nu = \mathcal{D}^2/\nu$ the viscous diffusion time, $\tau_\eta = \mathcal{D}^2/\eta$ the magnetic diffusion time, $\tau_T = \mathcal{D}^2/\kappa_T$ the thermal diffusion time and $\tau_\xi = \mathcal{D}^2/\kappa_\xi$ the chemical diffusion time.

Earth’s outer core evolves on a broad range of timescales, as one can glean from the inspection of Table 3. In particular, even if the evolution of temperature and composition are governed by similar transport equations (see eqs 5 and 6), thermal diffusion is much more efficient than chemical diffusion, which causes the Lewis number to greatly exceeds unity (see Table 2). This implies that the typical lengthscale of chemical heterogeneities is possibly several orders of magnitude smaller than the length scale of thermal heterogeneities. The values of the control parameters spanned by the simulations presented in this work are discussed in section 2.6.

2.3 Boundary conditions

The inner core is growing and is ejecting light elements because of its crystallization, which in principle yields coupled boundary conditions for temperature and composition (e.g. Glatzmaier & Roberts 1996; Anufriev *et al.* 2005). For the sake of simplicity, thermal and chemical boundary conditions are considered as decoupled here, as in for example Takahashi (2014). We consider two different setups to explore the impact of varying the thermal boundary conditions:

(i) *Fixed fluxes*: thermal and composition fluxes are imposed at both boundaries with

$$\begin{cases} \partial_r T(r_i) = -1, & \partial_r T(r_o) = 0, \\ \partial_r \xi(r_i) = -1, & \partial_r \xi(r_o) = 0. \end{cases} \quad (7)$$

(ii) *Hybrid*: temperature is fixed at the ICB while the temperature flux is imposed at the CMB, the boundary conditions on chemical composition are the same as in the previous setup

$$\begin{cases} T(r_i) = 0, & \partial_r T(r_o) = -1, \\ \partial_r \xi(r_i) = -1, & \partial_r \xi(r_o) = 0. \end{cases} \quad (8)$$

No-slip mechanical boundary conditions are used at both boundaries. The mantle is assumed to be insulating, such that the magnetic field at the CMB has to match a source-free potential field. The inner core is treated as a rigid electrically conducting sphere which can freely rotate around the \hat{z} -axis (e.g. Hollerbach 2000; Wicht 2002). Its rotation is a response to the viscous and magnetic torques exerted by the outer core on the inner core. The conductivity of the inner core is assumed to be equal to that of the outer core, and its

moment of inertia is calculated by using the same density as the liquid outer core.

2.4 Numerical approach

We solve the system of eqs (2)–(6) using the open-source geodynamo code MagIC¹ (Wicht 2002; Gastine *et al.* 2016). This code has been validated against a benchmark for double-diffusive convection initiated by Breuer *et al.* (2010).

The solenoidal vectors \mathbf{u} and \mathbf{B} are decomposed in poloidal and toroidal potentials

$$\begin{cases} \mathbf{u}(\mathbf{r}, t) = \nabla \times \nabla \times [W(\mathbf{r}, t)\hat{\mathbf{r}}] + \nabla \times [Z(\mathbf{r}, t)\hat{\mathbf{r}}], \\ \mathbf{B}(\mathbf{r}, t) = \nabla \times \nabla \times [G(\mathbf{r}, t)\hat{\mathbf{r}}] + \nabla \times [H(\mathbf{r}, t)\hat{\mathbf{r}}], \end{cases}$$

where \mathbf{r} is the radius vector. The new unknowns are then W , Z , G , H , T , ξ and p .

Each of these scalar fields is expanded in spherical harmonics to maximum degree and order ℓ_{\max} in the horizontal direction. The spherical harmonic representation of the magnetic poloidal potential G reads

$$G(r, \theta, \varphi, t) \simeq \sum_{\ell=0}^{\ell_{\max}} \sum_{m=-\ell}^{\ell} G_{\ell m}(r, t) Y_{\ell}^m(\theta, \varphi),$$

where $G_{\ell m}(r, t)$ is the coefficient associated to Y_{ℓ}^m , the spherical harmonic of degree ℓ and order m . The non-linear terms are calculated in physical space. The open-source SHTns library² (see Schaeffer 2013) is used to compute the forward and inverse spectral transforms on the unit-sphere.

In the radial direction, MagIC uses either a finite difference scheme, or a Chebyshev collocation method (see Boyd 2001). The finite difference grid, whose number of points is denoted by N_r , is regularly spaced in the bulk of the domain and follows a geometrical progression near the boundaries (see Dormy *et al.* 2004). When the collocation approach is selected, Chebyshev polynomials are truncated at degree N and the N_r collocation points r_k are defined by

$$\forall k \in \llbracket 1, N_r \rrbracket, \begin{cases} r_k = \frac{1}{2} [(r_o - r_i)x_k + r_o + r_i] \\ x_k = \cos \left[\frac{(k-1)\pi}{N_r - 1} \right]. \end{cases} \quad (9)$$

Due to the particular choice of spatial grid given by the equation above, the transforms between physical grid and Chebyshev representation are carried out by fast discrete cosine transform (see Press *et al.* 1992, chapter 12). This discretization yields a point densification close to the boundaries which could impose severe time step restrictions when the magnetic field is strong (see Christensen *et al.* 1999). To mitigate this effect, we adopt the mapping proposed by Kosloff & Tal-Ezer (1993) and replace x_k in eq. (9) by

$$\forall k \in \llbracket 1, N_r \rrbracket, X_k = \frac{\arcsin(\alpha x_k)}{\arcsin(\alpha)} \quad \text{with } \alpha \in]0, 1],$$

where α is the mapping coefficient. To maintain the spectral convergence of the simulation α has to verify

$$\alpha \leq \alpha_{\max} = \left\{ \cosh \left[\frac{|\ln(\epsilon)|}{N_r - 1} \right] \right\}^{-1}, \quad (10)$$

where ϵ is the machine precision.

¹<https://magic-sph.github.io/>

²<https://bitbucket.org/nschaeff/shtns>

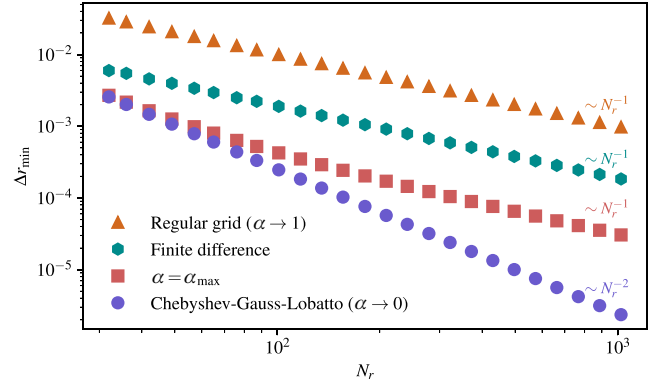


Figure 2. Minimal grid spacing Δr_{\min} between two radial points as a function of the number of collocation points N_r for a regularly spaced grid, the grid used when finite differences are used, the collocation grid with the mapping by Kosloff & Tal-Ezer (1993) with a mapping coefficient α_{\max} (eq. 10) and the standard Gauss–Lobatto grid.

Fig. 2 shows the minimum grid spacing Δr_{\min} as a function of N_r for a regular grid, the finite difference grid with geometrical clustering near the boundaries, and two collocation grids, with $\alpha \rightarrow 0$ (Gauss–Lobatto grid) and $\alpha = \alpha_{\max}$. Because $\Delta r_{\min} \sim N_r^{-2}$ when using the classical Gauss–Lobatto grid, adopting the mapping by Kosloff & Tal-Ezer (1993) yields a possible increase of Δr_{\min} by a factor 2–3 when $N_r \gtrsim 100$. The time step size could in principle rise by a comparable amount, should it be controlled by the propagation of Alfvén waves in the vicinity of the boundaries (Christensen *et al.* 1999). Using the finite difference method enables even larger grid spacing and hence possible additional gain in the time step size. This speed-up shall however be mitigated by the fact that N_r has to be increased by a factor 1.5–3 when using finite differences to achieve an accuracy comparable to that of the Chebyshev collocation method (see Christensen *et al.* 2001; Matsui *et al.* 2016).

$G_{\ell m}$ is then expanded in truncated Chebyshev series

$$G_{\ell m}(r_k, t) \simeq \sqrt{\frac{2}{N_r - 1}} \sum_{n=0}^{N-1} G_{\ell mn}(t) T_n(r_k), \quad (11)$$

with

$$G_{\ell mn}(t) \simeq \sqrt{\frac{2}{N_r - 1}} \sum_{n=1}^{N_r} G_{\ell m}(x_k, t) T_n(x_k),$$

where the double primes on the summations indicate that the first and the last indices are multiplied by one half (see Glatzmaier 1984). In the above equations, $T_n(x_k)$ is the n -th order Chebyshev polynomial at the collocation point x_k defined by

$$T_n(x_k) = \cos[n \arccos(x_k)] = \cos \left[\frac{\pi n(k-1)}{N_r - 1} \right].$$

Further details on spherical harmonics and Chebyshev polynomials expansion can be found in Tilgner (1999) and Christensen & Wicht (2015).

Once the spatial discretization has been specified, the set of eqs (2)–(6) complemented by the boundary conditions (see eqs 7 and 8) forms a semi-discrete system where only the time discretization remains to be expressed. As an example, the time evolution of the poloidal potential for the magnetic field $G_{\ell m}(r_k)$ (see eq. 11) can be written as an ordinary differential equation

$$\begin{cases} \frac{dG_{\ell m}}{dt}(r_k, t) = \mathcal{E}[\mathbf{u}, \mathbf{B}] + \mathcal{I}[G_{\ell m}], \\ G_{\ell m}(x_k, t_0) = G_{\ell m}^0(x_k), \end{cases} \quad (12)$$

where $G_{\ell m}^0(r_k)$ is the initial condition, \mathcal{E} a non linear-function of \mathbf{u} and \mathbf{B} and \mathcal{I} a linear function of $G_{\ell m}$. The above equation serves as a canonical example of the treatment of the different contributions: the non-linear terms are treated explicitly (function \mathcal{E}) while the remaining linear terms are handled implicitly (function \mathcal{I}). In MagIC, several implicit/explicit (IMEX) time schemes are used to time advance the set of eqs (2)–(6) from t to $t + \delta t$:

- (i) A combination of a Crank–Nicolson for the implicit terms and a second-order Adams–Bashforth for the explicit terms called CNAB2 (see Glatzmaier 1984).
- (ii) Two IMEX Runge–Kutta: PC2 (see Jameson *et al.* 1981) and BPR353 (see Boscarino *et al.* 2013).

CNAB2 has been commonly used in geodynamo models since the pioneering work of Glatzmaier (1984). IMEX Runge–Kutta schemes have been rarely used in the context of geodynamo models (Glatzmaier & Roberts 1996), rapidly rotating convection in spherical shells (Marti *et al.* 2016) or quasi-geostrophic models of 2-D convection (Gastine 2019). For IMEX Runge–Kutta schemes, s substages are solved to time-advance eq. (12) from t to $t + \delta t$

$$G_{\ell m}^i(r_k) = G_{\ell m}(r_k, t) + \delta t \sum_{j=0}^i (a_{i,j}^{\mathcal{E}} \mathcal{E}^j + a_{i,j}^{\mathcal{I}} \mathcal{I}^j), \quad (13)$$

where $i \in \llbracket 0, s \rrbracket$, $G_{\ell m}^i$ is the intermediate solution at substage i , $\mathcal{E}^j = \mathcal{E}[\mathbf{B}, \mathbf{u}](t + c_j^{\mathcal{E}} \delta t)$ and $\mathcal{I}^j = \mathcal{I}[G_{\ell m}](t + c_j^{\mathcal{I}} \delta t)$. $G_{\ell m}(r_k, t + \delta t)$ is then given by

$$G_{\ell m}(r_k, t + \delta t) = G_{\ell m}(r_k, t) + \delta t \sum_{j=0}^s (b_j^{\mathcal{E}} \mathcal{E}^j + b_j^{\mathcal{I}} \mathcal{I}^j) \quad (14)$$

In the above equations, the matrices $\mathbf{a}^{\mathcal{I}}$ and $\mathbf{a}^{\mathcal{E}}$ and the vectors $\mathbf{b}^{\mathcal{I}}$, $\mathbf{b}^{\mathcal{E}}$, $\mathbf{c}^{\mathcal{E}}$ and $\mathbf{c}^{\mathcal{I}}$ form the so-called Butcher tables of the IMEX Runge–Kutta schemes given in Appendix A. Since the last lines of $\mathbf{a}^{\mathcal{E}, \mathcal{I}}$ are equal to $\mathbf{b}^{\mathcal{E}, \mathcal{I}}$ for PC2 and BPR353, the last operation to retrieve $G_{\ell m}(r_k, t + \delta t)$ (eq. 14) is actually redundant with the last substage (see Ascher *et al.* 1997). IMEX Runge–Kutta schemes require more computational operations to time advance the set of eqs (2)–(6) from t to $t + \delta t$ than CNAB2. However, they allow larger time step sizes that compensate for this extra numerical cost (Marti *et al.* 2016) and they are more accurate and stable. Since BPR353 is a third-order scheme, it is particularly attractive to ensure an accurate equilibration of the most turbulent runs.

2.5 Simulation diagnostics

For each diagnostic quantity f , we adopt in the following overbars for time averaging and angle brackets for spatial averaging

$$\bar{f} = \frac{1}{t_{\text{avg}}} \int_{t_0}^{t_0+t_{\text{avg}}} f(t) dt \quad \text{and} \quad \langle f \rangle_V = \frac{1}{V} \int_V f(\mathbf{r}, t) dV,$$

where t_{avg} corresponds to the averaging time.

2.5.1 Integral quantities and scales

The magnetic E_m and kinetic E_k energies are given by

$$E_m(t) + E_k(t) = \frac{1}{2} \left[\int_{V_o+V_i} \frac{\mathbf{B}^2(\mathbf{r}, t)}{E P m} dV + \int_{V_o} \mathbf{u}^2(\mathbf{r}, t) dV \right],$$

where V_i is the inner core volume. By multiplying the Navier–Stokes eq. (3) by \mathbf{u} and the induction eq. (4) by \mathbf{B} , we obtain the following

power balance:

$$\frac{d}{dt} (E_k + E_m)(t) = P_T(t) + P_{\xi}(t) - D_v(t) - D_{\eta}(t).$$

In the case of double-diffusive convection, the energy is provided by chemical and thermal buoyancy power P_{ξ} and P_T defined by

$$\begin{cases} P_{\xi}(t) = V_o \left\langle \frac{R a_{\xi}}{S c} \xi(\mathbf{r}, t) \frac{r}{r_o} u_r(\mathbf{r}, t) \right\rangle_{V_o} \\ P_T(t) = V_o \left\langle \frac{R a_T}{P r} T(\mathbf{r}, t) \frac{r}{r_o} u_r(\mathbf{r}, t) \right\rangle_{V_o} \end{cases}$$

and dissipated by viscous and Ohmic dissipations D_v and D_{η} given by

$$\begin{cases} D_v(t) = V_o \langle [\nabla \times \mathbf{u}(\mathbf{r}, t)]^2 \rangle_{V_o} \\ D_{\eta}(t) = (V_o + V_i) \left\langle \frac{[\nabla \times \mathbf{B}(\mathbf{r}, t)]^2}{E P m^2} \right\rangle_{V_o+V_i} \end{cases}.$$

Once a statistically steady state has been reached, the input buoyancy powers should compensate the Ohmic and viscous dissipations. Following King *et al.* (2012), to assess the consistency of the numerical computations, we measure the time-average difference between input and output powers ΔP

$$\Delta P = 100 \times \frac{\overline{P_T + P_{\xi} - D_v - D_{\eta}}}{\overline{P_T + P_{\xi}}}.$$

We made sure that this difference remained lower than 1.5 per cent for all the simulations reported in this study. This value is below the 2 per cent threshold considered as sufficient to ensure the convergence of integral diagnostics (see King *et al.* 2012; Gastine *et al.* 2015). For each simulation, the total convective power P^{tot} and the relative thermal convective power $P_T^{\%}$ are defined by

$$P^{\text{tot}} = \overline{P_T(t) + P_{\xi}(t)} \quad \text{and} \quad P_T^{\%} = \frac{\overline{P_T(t)}}{\overline{P_T(t) + P_{\xi}(t)}} \times 100. \quad (15)$$

$P_T^{\%}$ hence vanishes for a purely chemical forcing and is equal to 100 per cent for a purely thermal forcing.

Following Christensen & Aubert (2006) and Schwaiger *et al.* (2019), we introduce two quantities to characterize the typical flow lengthscale. The integral scale L already discussed in the introduction is obtained from the time-averaged kinetic energy spectrum

$$L = \pi \frac{\overline{2E_k(t)}}{\sum_{\ell} \ell \overline{\mathbf{u}^{\ell}(t) \cdot \mathbf{u}^{\ell}(t)}},$$

where $\overline{\mathbf{u}^{\ell} \cdot \mathbf{u}^{\ell}}/2$ is the kinetic energy contained in spherical harmonic degree ℓ , while the dominant lengthscale $\hat{\ell}$ is defined as the peak of the poloidal kinetic energy spectra (Schwaiger *et al.* 2019, 2021)

$$\hat{\ell} = \text{argmax}_{\ell} \left[E_{k,p}^{\ell}(t) \right],$$

where $E_{k,p}^{\ell}$ is the contribution of spherical harmonic degree ℓ to the total poloidal kinetic energy.

In order to explore the impact of the equatorial symmetry of the flow on the dipole–multipole transition, we consider the relative equatorially symmetric kinetic energy ζ introduced by Garcia *et al.* (2017)

$$\zeta = \frac{\overline{E_k^{\text{s,NZ}}}}{\overline{E_k^{\text{NZ}}}}, \quad (16)$$

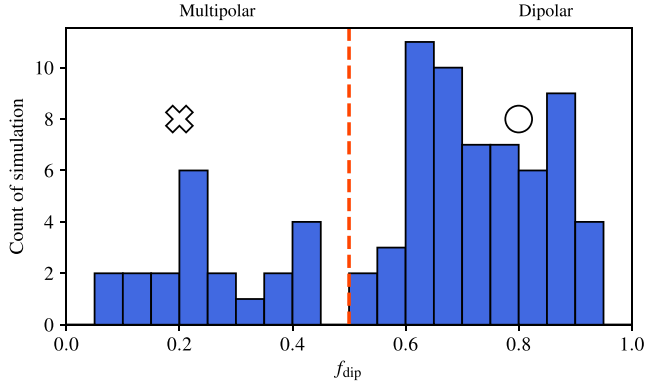


Figure 3. Distribution of the dipolar fraction f_{dip} for the 79 numerical simulations of this study. Multipolar simulations are defined as having $f_{\text{dip}} < 0.5$, and they will be marked by a cross in subsequent figures. Dipolar simulations ones will be displayed using a circle. The vertical dashed line marks the $f_{\text{dip}} = 0.5$ limit between dipolar and multipolar simulations.

where E_k^{NZ} is the kinetic energy contained in the non-zonal flow and $E_k^{\text{S,NZ}}$ the kinetic energy contained in the equatorially symmetric part of the non-zonal flow.

We measure the mean convective flow amplitude either by the magnetic Reynolds number Rm or by the Rossby number Ro defined by

$$Rm = \frac{\sqrt{2E_k(t)}Pm}{\tau_{\text{adv}}} = \frac{\tau_\eta}{\tau_{\text{adv}}}, \quad Ro = \frac{\sqrt{2E_k(t)}E}{\tau_{\text{adv}}} = \frac{\tau_\Omega}{\tau_{\text{adv}}},$$

where $\tau_{\text{adv}} = \mathcal{D}/u_{\text{rms}}$ is the characteristic turnover time and u_{rms} the root mean square flow velocity. Following Christensen & Aubert (2006), we define a local Rossby number by

$$Ro_L = Ro \frac{\mathcal{D}}{L}.$$

The dipolar character of the CMB magnetic field is quantified by its dipolar fraction f_{dip} , defined as the ratio of the axisymmetric dipole component to the total field strength at the CMB in spherical harmonics up to degree and order 12.

Fig. 3 shows the statistical distribution of f_{dip} for the simulations reported in this study. Two distinct groups of numerical simulations separated by a gap at $f_{\text{dip}} \approx 0.5$ are visible in this figure. A magnetic field is considered as dipolar when $f_{\text{dip}} > 0.5$ and multipolar otherwise. This bound differs from the original threshold of $f_{\text{dip}} = 0.35$ considered by Christensen & Aubert (2006), but it is found to better separate the two types of dynamo models contained in our data set. Note that the same bound of 0.5 was recently chosen by Menu *et al.* (2020) in their study. The magnetic field amplitude is measured by the Elsasser number Λ

$$\Lambda = \sqrt{2E_m}.$$

Finally, transports of heat and chemical composition are quantified by using the Nusselt Nu and the Sherwood Sh number defined by (see Goluskin 2016, chapter 1)

$$Nu = \frac{\Delta T_0}{\Delta T} \quad \text{and} \quad Sh = \frac{\Delta \xi_0}{\Delta \xi},$$

where ΔT , $\Delta \xi$ are the temperature and composition differences between the ICB and the CMB, and the subscript 0 stands for the background conducting state. For both the fixed fluxes and hybrid configurations (recall Section 2.3), we obtain a background composition contrast given by

$$\Delta \xi_0 = \frac{\eta(\eta + 2)}{2(\eta^2 + \eta + 1)}, \quad (17)$$

where $\eta = r_i/r_o$ is the radius ratio. The background temperature drop ΔT_0 depends on the imposed boundary conditions. For the fixed flux setup, it reads

$$\Delta T_0^{\text{ff}} = \frac{\eta(\eta + 2)}{2(\eta^2 + \eta + 1)} = \Delta \xi_0, \quad (18)$$

while it becomes

$$\Delta T_0^{\text{hyb}} = \frac{1}{\eta}, \quad (19)$$

for the hybrid setup.

Table 4 gives the definition of most of these integral diagnostics and provides estimates for Earth's core, along with the bracket of values obtained in the numerical data set presented here.

2.6 Exploration of parameter space

We compute 79 simulations varying the Ekman number, the magnetic Prandtl number, the thermal and the chemical Rayleigh numbers. The properties of this data set are listed in Table A1. The less turbulent simulations have been initialized with a strong dipolar field and a random thermochemical perturbation. Their final states have been used as initial conditions for the more turbulent simulations, in order to shorten their transients. Three different Ekman numbers are considered in this study: 10^{-4} , 3×10^{-5} and 10^{-5} . Ra_T has been varied between 0 and 6×10^{10} and Ra_ξ between 0 and 1.9×10^{12} to study the influence of the convective forcing and span the transition between dipole-dominated and multipolar dynamos. We adopt $Pr = 0.3$ and $Sc = 3$ (i.e. $Le = 10$) for a better comparison with previous studies (e.g. Takahashi 2014) and to mitigate the computational cost associated with large Lewis numbers. Pm varies between 0.5 and 7, depending on the Ekman number, in order to maintain $Rm > 100$. The numerical models were integrated for at least 20 per cent of a magnetic diffusion time τ_η for the most turbulent (and demanding) ones, and for more than one τ_η for the others, in order to ensure that a statistically steady state has been reached.

3 RESULTS

3.1 Onset of top-heavy convection

Fig. 4 shows the location of the 79 computed numerical simulations for the three considered Ekman numbers in the parameter space ($\mathcal{G}_T, \mathcal{G}_\xi$) defined by

$$\mathcal{G}_T = 1 + Gr_T E^{4/3} \quad \text{and} \quad \mathcal{G}_\xi = 1 + Gr_\xi E^{4/3},$$

where $Gr_{T(\xi)}$ corresponds to the thermal (chemical) Grashof number,

$$Gr_T = \frac{Ra_T}{Pr} \quad \text{and} \quad Gr_\xi = \frac{Ra_\xi}{Sc}.$$

Adding 1 to $Gr_{T(\xi)} E^{4/3}$ in the above equations allows us to use logarithmic scales in the top row of Fig. 4.

We determine the onset of convection using the open-source software SINGE³ which computes linear eigenmodes for incompressible, double-diffusive fluids enclosed in a spherical cavity (see Schaeffer 2013; Vidal & Schaeffer 2015; Kaplan *et al.* 2017; Monville *et al.* 2019). For a fixed Ra_T (Ra_ξ), the code solves the generalized

³<https://bitbucket.org/vidalje/singe>

Table 4. Output parameters of the numerical simulations and their estimates for Earth's core.

Name	Symbol	Definition	Earth's core	This study	References
Relative thermal convective power	$P_T^{\%}$	see eq. (15)	20–70 %	0–100 %	Lister & Buffett (1995) - Takahashi (2014)
Rossby	Ro	$u_{\text{rms}}/\Omega D$	$(1.7\text{--}12) \times 10^{-6}$	0.002–0.1	Table 1
Local Rossby	Ro_L	$u_{\text{rms}}/\Omega L$	$4.7 \times 10^{-5} - 0.09$	0.009–0.45	Davidson (2013) - Olson & Christensen (2006)
Relative equat. symmetric kinetic energy	ζ		0.78–0.9	0.65–0.96	Aubert <i>et al.</i> (2017)
Magnetic Reynolds	Rm	$u_{\text{rms}}D/\eta$	$(0.2\text{--}9) \times 10^3$	$10^2\text{--}6 \times 10^3$	Table 1
Elsasser	Λ	$B_{\text{rms}}^2/\mu_0\eta\rho_o\Omega$	6.7–39	$0.3\text{--}3 \times 10^2$	Table 1
Dipolarity parameter	f_{dip}		0.6–0.7	0.1–1	Gillet <i>et al.</i> (2015)

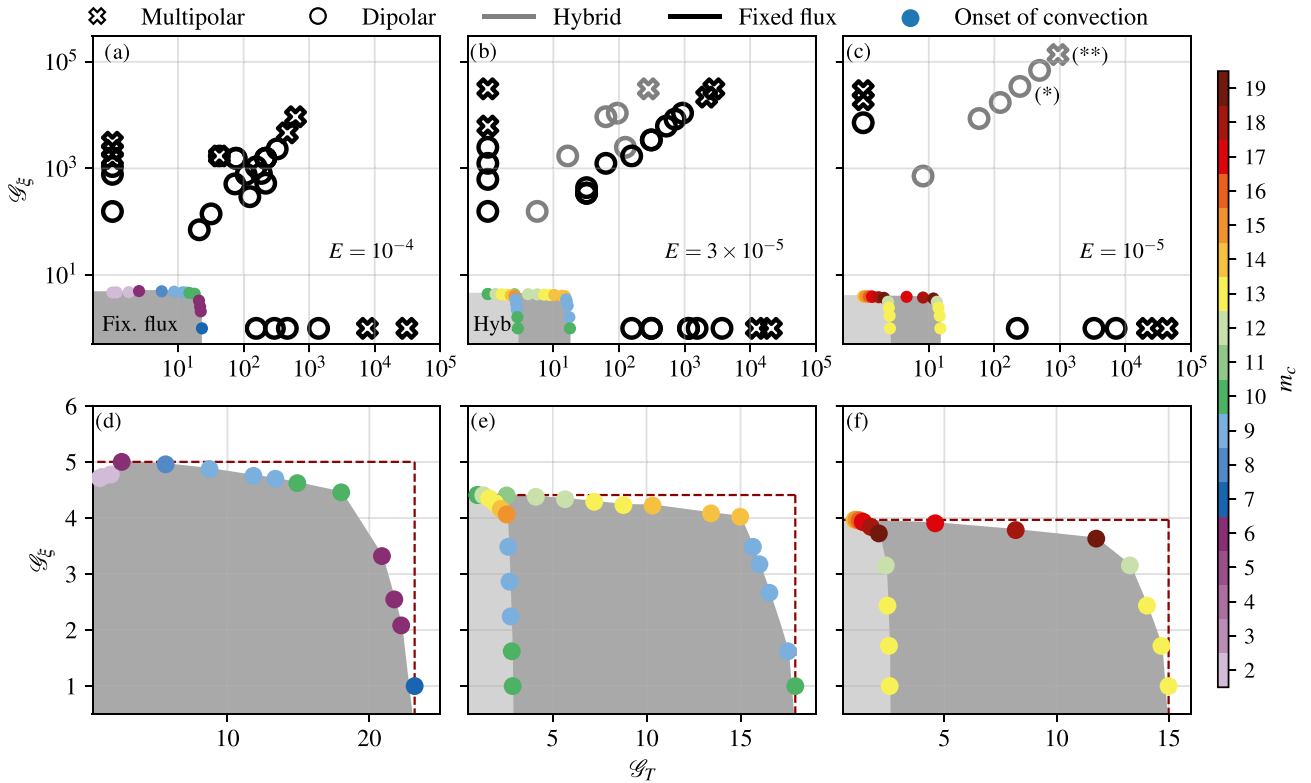


Figure 4. Linear onset of top-heavy convection in $(1 + Gr_T E^{4/3}, 1 + Gr_\xi E^{4/3})$ parameter space, where Gr_T , Gr_ξ and E are the thermal Grashof, chemical Grashof and Ekman numbers E considered in this study: 10^{-4} (left-hand column), 3×10^{-5} (centre column) and 10^{-5} (right-hand column). Critical curves correspond to the edges of the gray shaded areas. Dark grey areas were obtained for fixed-flux boundary conditions and light gray areas for hybrid boundary conditions, the latter present only for $E = 3 \times 10^{-5}$ and $E = 10^{-5}$. The bottom panels (d), (e) and (f) show zoomed-in insets of upper panels (a), (b) and (c). The edges of the gray areas, which define the critical curves, connect discs whose colour defines the critical azimuthal wavenumber m_c . The top row (in logarithmic scale in both directions) also features the location of the 79 simulations computed in this study. Circles (resp. crosses) represent dipolar (resp. multipolar) simulations. Circles and crosses with gray (resp. black) edges correspond to fixed-flux (resp. hybrid) boundary conditions. Simulations (*) and (**) are reference simulations discussed in detail in the text (see also Table A1).

eigenvalue problem formed by the linearized Navier–Stokes and transport equations. It seeks eigenmodes f of the form

$$f(t, r, \theta, \varphi) = \hat{f}(r, \theta) \exp[i(m\varphi - \omega t)],$$

where \hat{f} is a function of r and θ , m is the azimuthal wave number and ω the complex angular frequency. Starting at a specific (Ra_T, Ra_ξ) , the critical mode is determined by varying one of the Rayleigh numbers (keeping the other fixed) in order to obtain an ω with a vanishing imaginary part. The onset mode is then characterized by its critical chemical and thermal Rayleigh numbers (Ra_ξ^c, Ra_T^c) , its critical azimuthal wave number m_c and its (real) angular drift frequency ω_c . Connecting the (Ra_ξ^c, Ra_T^c) pairs that we collected

with SINGE gives rise to the critical curves plotted in Fig. 4. In each panel, the intersection of these curves with the x -axis (resp. y -axis) corresponds to the critical Rayleigh number for purely thermal (resp. chemical) convection. Underneath the critical curves, the grey-shaded areas are regions of the parameter space where thermal and chemical perturbations are unable to trigger a convective flow.

We note that the shape delimited by the critical curves in the bottom row of Fig. 4 is not rectangular, as would be the case if the two sources of buoyancy were independent. Instead, we observe a decrease of the critical Gr_ξ^c when Gr_T^c increases for the three different Ekman numbers. As previously reported by Busse (2002), Trümper *et al.* (2012) and Net *et al.* (2012), and discussed in Section 1,

this demonstrates that the addition of a second buoyancy source facilitates the onset of convection as compared to the single diffusive configurations.

Starting from $\mathcal{G}_T^c = 0$ and following the critical curve for each Ekman number, m_c grows until one reaches the upper right ‘corner’ of the onset region and then decreases to a value comparable to the starting $\mathcal{G}_T^c = 0$ m_c value when \mathcal{G}_ξ^c tends to zero. We observe that m_c is nearly constant on the vertical branches, while it increases much faster on the horizontal ones, as already reported by Trümper *et al.* (2012).

As can be seen in Figs 4(e) and (f), the shaded shape is much wider with fixed-flux boundary conditions than with hybrid boundary conditions. This comes from the difference in the temperature contrasts of the background conducting states. An adequate way to compare both setups resorts to using *diagnostic* Grashof numbers

$$\widetilde{Gr}_T = Gr_T \Delta T_0, \quad \widetilde{Gr}_\xi = Gr_\xi \Delta \xi_0, \quad (20)$$

that are based on the temperature (composition) contrasts ΔT_0 ($\Delta \xi_0$) of the reference conducting state instead of the *control* thermal (chemical) Grashof numbers Gr_T (Gr_ξ) (see Johnston & Doering 2009; Goluskin 2016). Using eqs (18) and (19), the temperature difference between ICB and CMB for the conducting states for both setups reads

$$\frac{\Delta T_0^{\text{hyb}}}{\Delta T_0^{\text{ff}}} = \frac{2(\gamma^2 + \gamma + 1)}{\gamma^2(\gamma + 1)} \approx 10.23,$$

which is in good agreement with the actual ratio of critical \mathcal{G}_T^c observed in panels (e) and (f) of Fig. 4.

The analysis of the onset of double-diffusive convection becomes even more straightforward if one adopts the formalism introduced by Silva *et al.* (2019). This framework rests on two parameters: first, the *diagnostic effective Grashof number*

$$\widetilde{Gr}_c = \sqrt{(\widetilde{Gr}_T^c)^2 + (\widetilde{Gr}_\xi^c)^2}, \quad (21)$$

and second the *Grashof mixing angle* Θ such that

$$\cos \Theta = \frac{\widetilde{Gr}_T^c}{\widetilde{Gr}_c}, \quad \sin \Theta = \frac{\widetilde{Gr}_\xi^c}{\widetilde{Gr}_c}. \quad (22)$$

The pair $(\widetilde{Gr}_c, \Theta)$ can be interpreted as the polar coordinates of the critical onset mode in the $(\widetilde{Gr}_T, \widetilde{Gr}_\xi)$ Cartesian parameter space. A mixing angle $\Theta = 0$ hence corresponds to purely thermal convection, while $\Theta = \pi/2$ corresponds to purely chemical convection. Fig. 5 shows the critical effective Grashof number \widetilde{Gr}_c , the critical azimuthal wave number m_c and the critical angular drift frequency $|\omega_c|$, multiplied in each instance by their expected asymptotic dependence on the Ekman number for purely thermal convection, as a function of the Grashof mixing angle Θ . Adopting a diagnostic effective Grashof number conveniently enables the merging of the onset curves associated with the two sets of thermal boundary conditions (fixed-flux and hybrid).

The onset curves can be separated into two branches: (i) From $\Theta = 0$ up to $\Theta \approx \pi/16$, the onset mode almost behaves as a pure low- Pr thermal mode with little change in $m_c E^{1/3}$ and a large drift speed; (ii) a sharp transition to another kind of onset mode, reminiscent of the $Pr \gtrsim 1$ convection onset, is observed for $\Theta \gtrsim \pi/16$. The latter is characterized by a smaller drift frequency, a higher azimuthal wavenumber and a lower effective Grashof number \widetilde{Gr}_c . The critical azimuthal wavenumber reaches its maximum for $\Theta \approx \pi/16$ before gradually decreasing to reach a value comparable to that expected for purely thermal convection towards $\Theta = \pi/2$.

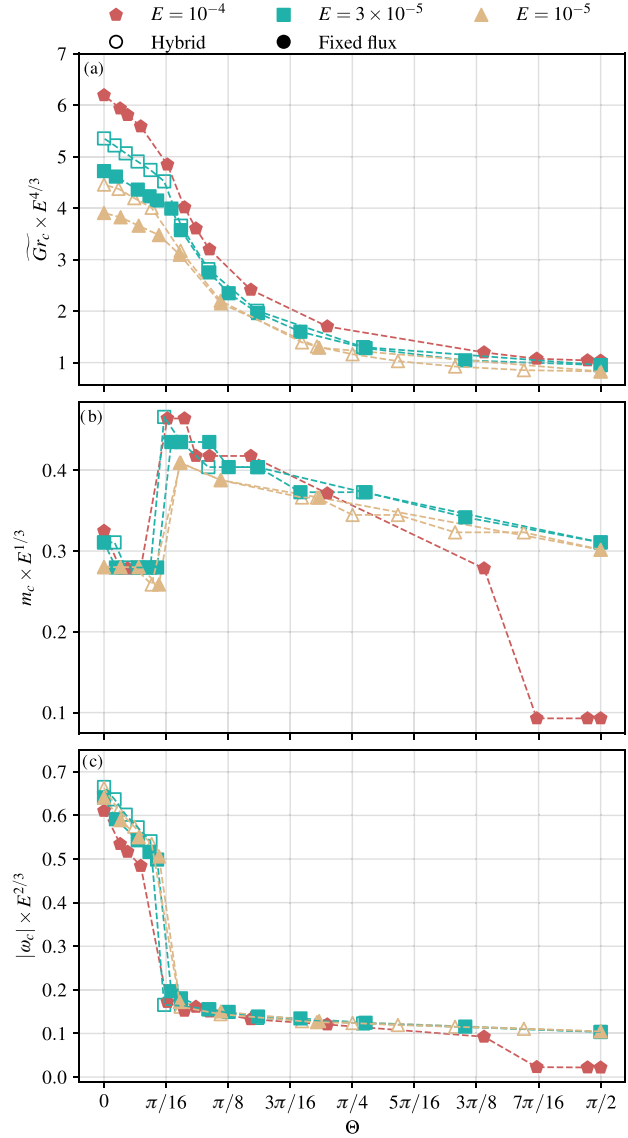


Figure 5. (a) Critical effective Grashof number multiplied by $E^{4/3}$ as a function of the Grashof mixing angle Θ . (b) Critical azimuthal wavenumber m_c multiplied by $E^{1/3}$ as a function of Θ . (c) Critical drift frequency ω_c multiplied by $E^{2/3}$ as a function of Θ . Symbol colours correspond to the Ekman number, open-symbols to hybrid boundary conditions and filled symbols to fixed-flux boundary conditions.

The Ekman dependence is almost perfectly captured by the asymptotic scalings $E^{-1/3}$ and $E^{-2/3}$ for the critical wavenumber m_c and the drift frequency ω_c . The case of mixing angles $\Theta \geq 7\pi/16$ with $E = 10^{-4}$ constitutes an exception to this rule with a sharp drop to a constant critical wavenumber $m_c = 2$ (see the small kink in the upper left part of Fig. 4d). The dependence of \widetilde{Gr}_c on the Ekman number shows a more pronounced departure from the leading-order asymptotic scaling $Gr_c \sim E^{-4/3}$. As shown by Dormy *et al.* (2004) for differential heating (see e.g. their Fig. 5), the higher-order terms in the asymptotic expansion of Ra_T^c as a function of the Ekman number are still significant for $E > 10^{-6}$ (see also Schaeffer 2016). Given the range of Ekman numbers considered for this study, it is not surprising that the asymptotic scaling for Gr_c is not perfectly realized yet.

In summary, the onset of double-diffusive convection in the top-heavy regime takes the form of thermal-like drifting Rossby waves, the nature of which strongly depends on the fraction between chemical and thermal forcings. This confirms the results previously obtained by Silva *et al.* (2019, their fig. 9).

3.2 A reference case

We will now focus on the simulation marked by an asterisk (*) in Table A1 and in Fig. 4 to highlight specific double-diffusive convection features. This simulation corresponds to $Ra_T = 3.4 \times 10^8$, $Ra_\xi = 4.8 \times 10^{11}$, $E = 10^{-5}$ and $Pm = 0.5$ with hybrid boundary conditions. The thermal convective power amounts on average for 46 per cent of the total input power. Since the local Rossby number Ro_L reaches 0.11, this simulation is expected to operate in a parameter regime close to the transition between dipolar and multipolar regimes ($Ro_L \approx 0.12$) as put forward by Christensen & Aubert (2006). This high value of Ro_L also indicates the sizeable role played by inertia in the force balance of this simulation. Fig. 6 shows 3-D renderings of several fields extracted from a snapshot taken over the course of the numerical integration: (a) temperature perturbation, (b) composition, (c) zonal velocity and magnitude of

the velocity vector and (d) radial magnetic field and magnitude of the magnetic field vector. We chose the radius of the inner and outer spheres of these renderings to place ourselves outside thermal and compositional boundary layers. Convection is primarily driven by the chemical composition flux at the ICB. Because of the contrast in diffusion coefficients ($Le = 10$), compositional plumes develop at a much smaller scale than that of thermal plumes (see Figs 6a and b). Having $Le = 10$ also induces a chemical boundary layer much thinner than the thermal one, as illustrated by the Sherwood number Sh being five times larger than the Nusselt number Nu in this case (44.8 versus 8.0, see Table A1). The emission of a thermal plume is likely triggered by an impinging chemical plume. Accordingly, one would expect temperature fluctuations to be enslaved to compositional fluctuations, which may explain the outstanding spatial correlation between temperature and composition notable in Figs 6(a) and (b). This correlation was already reported by Trümper *et al.* (2012) for predominantly thermal convection.

In typical dipole-dominated dynamos, the velocity field features extended sheet-like structures that span most of the core volume (see Yadav *et al.* 2013; Schwaiger *et al.* 2019). Because of the strong forcing that characterizes the reference simulation, the convective flow is organized on smaller scales, which likely reflects

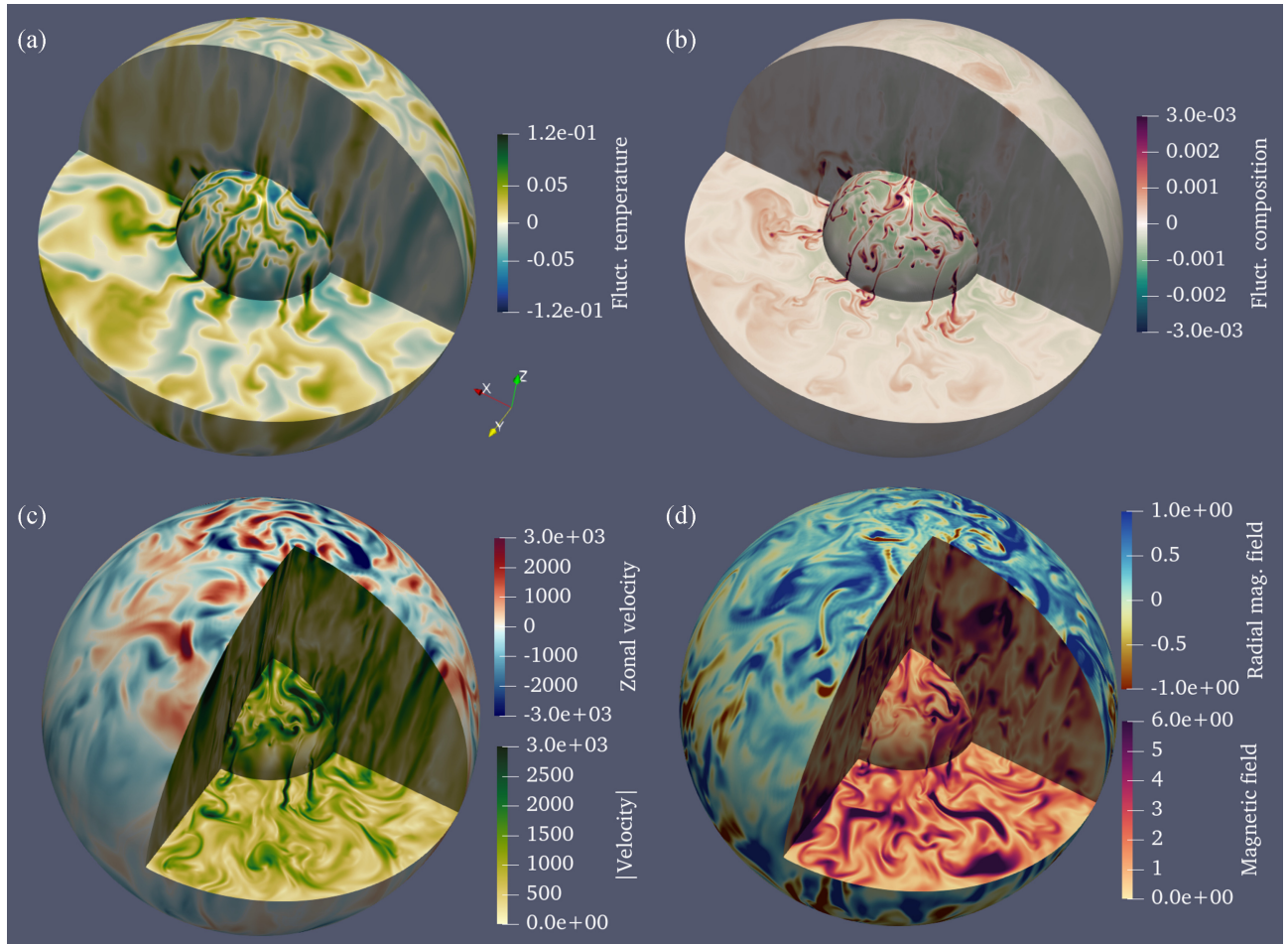


Figure 6. 3-D renderings of a snapshot of simulation (*) (see Table A1). On each panel, the inner and outer spherical surfaces correspond to dimensionless radii $r = 0.57$ and $r = 1.5$, respectively. The z -axis displayed in panel (a) corresponds to the axis of rotation. (a) Temperature perturbation. (b) Composition. (c) Velocity. The outer surface shows the zonal velocity u_φ , while the inner surface, the equatorial cut and the two meridional cuts display the magnitude of the velocity field, $|\mathbf{u}|$. (d): Magnetic field. The outer surface shows the radial field B_r , while the inner surface, the equatorial cut and the two meridional cuts display the magnitude of the magnetic field, $|\mathbf{B}|$. All fields are dimensionless.

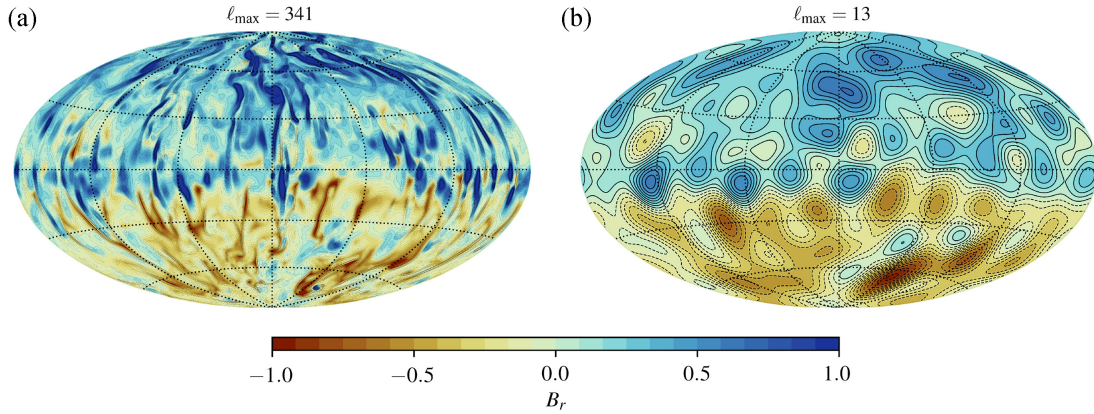


Figure 7. Hammer projection of the dimensionless radial magnetic field at the CMB truncated at the spherical harmonic degree $\ell_{\max} = 341$ (a) and at spherical harmonic degree $\ell_{\max} = 13$ (b) for the numerical simulation (*) shown in Fig. 6. It corresponds to the same snapshot as in Fig. 6. The dashed lines in panel(b) correspond to negative values of the radial magnetic field.

the sizeable amplitude of inertia. The magnetic field is dominated by its axisymmetric dipolar component (see Fig. 7a), despite the supposed proximity of the simulation with the dipolar–multipolar transition zone. Inspection of Table A1 indicates that this snapshot-based observation can in fact be extended to the entire duration of the simulation (close to half a magnetic diffusion time), as the average dipolar fraction f_{dip} is equal to 0.77.

The radial magnetic field features intense localized flux patches of mostly normal polarity in each hemisphere, with a few reverse flux patches paired with normal ones, mostly at high latitudes. Those fluid regions hosting a locally strong magnetic field are characterized by more quiescent flows, as can be seen in the equatorial planes of Figs 6(c) and (d) in the vicinity of the outer boundary. In a global sense, our reference simulation can be qualified as a *strong-field* dynamo since the ratio of the magnetic energy E_m to kinetic energy E_k is slightly larger than unity, $E_m/E_k = 1.36$.

Fig. 7 shows a comparison between the radial component of the magnetic field at the CMB (left-hand panel) and its representation truncated at spherical harmonic degree $\ell_{\max} = 13$ (right-hand panel). The truncated field presents several key similarities with the geomagnetic field at the CMB, such as a significant axial dipole and patches of reverse polarity in both hemispheres.

3.3 Earth-likeness

For a more quantitative assessment of the Earth-likeness of the dynamo models, we employ the rating of compliance χ^2 introduced by Christensen *et al.* (2010). This quantity is derived from four criteria based on the magnetic field at the CMB truncated at the degree $\ell = 8$

- (i) The relative axial dipole energy AD/NAD , which corresponds to the ratio of the magnetic energy in the axial dipole field to that of the rest of the field up to degree and order eight.
- (ii) The equatorial symmetry O/E corresponding to the ratio of the magnetic energy at the CMB of components that have odd values of $(\ell + m)$ for harmonic degrees between two and eight to its counterpart in components with $\ell + m$ even.
- (iii) The zonality Z/NZ , which corresponds to the ratio of the zonal to non-zonal magnetic energy for harmonic degrees two to eight at the CMB.
- (iv) The flux concentration factor FCF , defined by the variance in the squared radial field.

Table 5. Time-average of the rating parameters defined by Christensen *et al.* (2010) for Earth and the simulation (*) (see Table A1).

Name	Earth's value	Simulation (*)
AD/NAD	1.4	2.69
O/E	1.0	1.75
Z/NZ	0.15	0.25
FCF	1.5	1.46

To evaluate these quantities for the Earth, Christensen *et al.* (2010) used different models based on direct measures such as *gufm1* model by Jackson *et al.* (2000) and IGRF-11 model (from Finlay *et al.* 2010), as well as archeomagnetic and lake sediment data (model CALS7K.2 from Korte *et al.* 2005) and a statistical model for palaeofield (see Quidelleur & Courtillot 1996). These models allow to estimate the evolution of the mean value of the Gauss coefficients and their variances. Finally, they obtained the values given in Table 5 for the four rating parameters.

These values are used to determine the rating of compliance between numerical dynamo models and the geomagnetic field χ^2 expressed by

$$\chi^2 = \sum_{\psi_k} \left\{ \frac{\ln(\overline{\psi}_k) - \ln(\psi_k^{\oplus})}{\ln[\sqrt{\text{Var}(\psi_k^{\oplus})}]} \right\}^2,$$

where $\psi_k \in \{AD/NAD, O/E, Z/NZ, FCF\}$, $\text{Var}(\psi_k^{\oplus})$ is the variance of ψ_k^{\oplus} and the exponent \oplus stands for the Earth core. The agreement between simulation and Earth is termed by Christensen *et al.* (2010) as *excellent* if $\chi^2 < 2$, as *good* when $2 \leq \chi^2 \leq 4$, as *marginal* when $4 < \chi^2 \leq 8$ and *non-compliant* when $\chi^2 > 8$. We adopt the same classification in the following. According to Table 5, the relative axial dipole power (AD/NAD) and the equatorial symmetry (O/E) of the reference simulation (*) are too large in comparison with the reference geomagnetic values, which penalizes the overall compliance of the simulation. Nevertheless, the simulation remains in excellent agreement with the geomagnetic field with $\chi^2 = 1.5$.

Based on this rating of compliance χ^2 , Christensen *et al.* (2010) propose a representation to classify the different numerical dynamos according to the ratio of three different timescales: the rotation period τ_{Ω} , the advection time τ_{adv} and the magnetic diffusion time τ_{η} . Those can be cast into two dimensionless numbers: the magnetic Reynolds number Rm defined by $\tau_{\eta}/\tau_{\text{adv}}$ and the magnetic Ekman number E_{η} defined by $\tau_{\Omega}/\tau_{\eta} = E/Pm$. Fig. 8 shows our

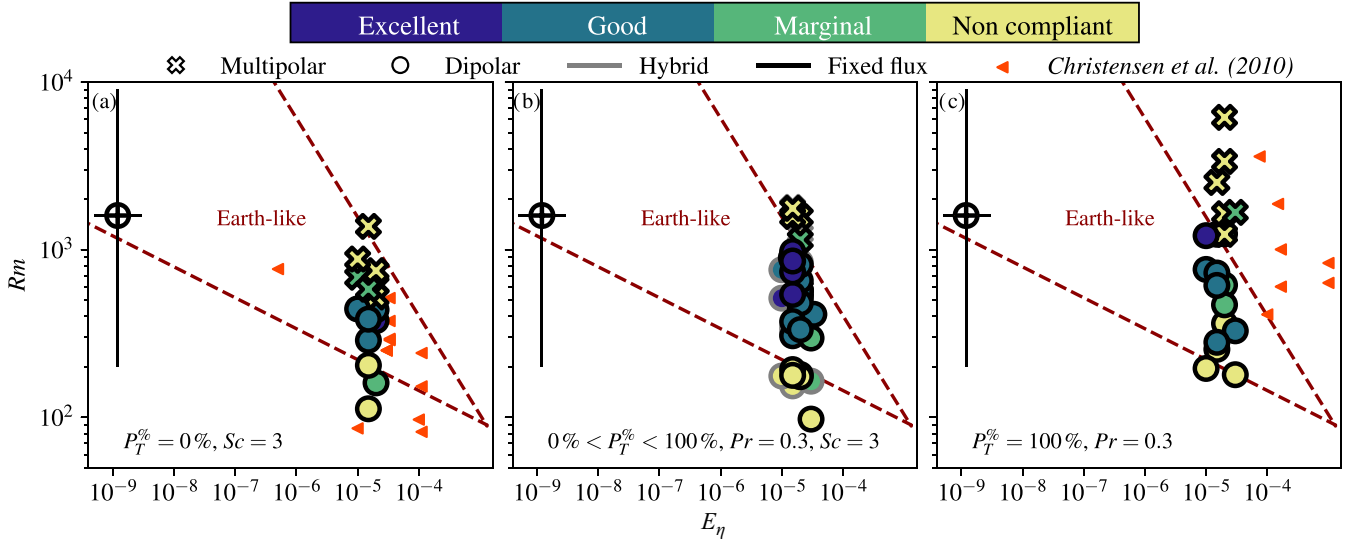


Figure 8. Compliance parameter χ^2 as a function of the magnetic Ekman number E_η and of the magnetic Rayleigh number Rm for three different setups: purely chemical convection (left-hand panel), double-diffusive convection (centre panel) and pure thermal convection (right-hand panel). Dashed lines mark the limits of the Earth-like domain defined by Christensen *et al.* (2010) and the black symbol \oplus marks the approximate position of the Earth's dynamo in this representation. The significant size of the error bars is due to the wide range of estimates for u_{rms} and η (see Table 2). The triangles correspond to the simulations provided by Christensen *et al.* (2010) with $Pr = 0.3$ or $Sc = 3$.

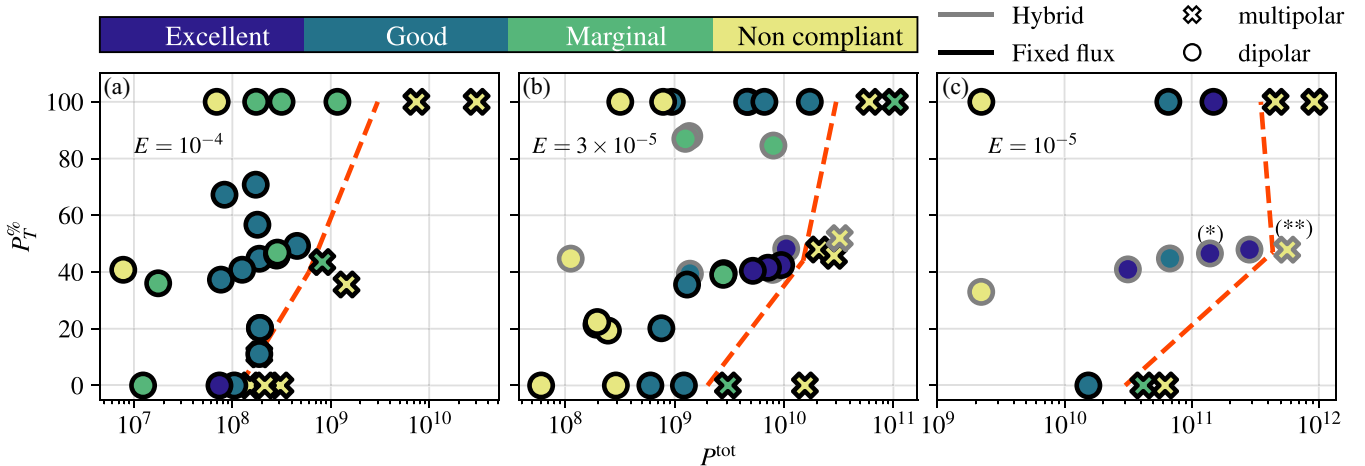


Figure 9. Compliance parameter χ^2 as a function of the input power P^{tot} and of the relative thermal buoyancy power $P_T^{\%}$ for the three different Ekman numbers considered in this study. The different colours correspond to the compliance quality defined by Christensen *et al.* (2010). The dashed lines mark a tentative extrapolation of the transition between dipolar and multipolar dynamos in this parameter space.

numerical simulations plotted in the parameter space (E_η , Rm). For comparison purposes, the simulations by Christensen *et al.* (2010) with $Pr = 0.3$ or $Sc = 3$ (triangular markers) have been added to our 79 dynamo models. To single out the effect of the diffusivities, the purely chemical, the double-diffusive and the purely thermal simulations have been plotted separately. The black symbol marks the approximate position of Earth's dynamo in this representation (see Tables 1 and 4). Christensen *et al.* (2010) posited the existence, in this parameter space, of a triangular wedge (delimited by dashed lines in Fig. 8), inside which the numerical dynamos yield Earth-like surface magnetic fields (those from our data set are shown in Fig. 8 with dark blue and blue disks for Excellent and Good ratings, respectively). Below the wedge, weakly supercritical dynamos feature too dipolar magnetic fields, on the account of the modest value of the magnetic Reynolds number. Conversely, a significant increase of the input power at a given E_η yields small-scale convective flows,

which possibly lead to the breakdown of the axial dipole (multipolar simulations displayed with crosses in Fig. 8). We observe in Fig. 8 that the upper boundary of the wedge actually depends on the value of $P_T^{\%}$: while several purely chemical simulations are already multipolar below $Rm \simeq 500$, the transition to multipolar dynamos is delayed to $Rm > 1500$ for the purely thermal ones. Although all those dynamo models that possess a good or excellent semblance with the geomagnetic field at the CMB lie within the boundaries of the original wedge, having a pair (E_η , Rm) that lies within this wedge cannot be considered as a sufficient condition to produce an Earth-like magnetic field, since the wedge includes a number of simulations with marginal or poor semblance.

To further discuss the impact of $P_T^{\%}$ on the morphology of the magnetic field at the CMB, Fig. 9 shows χ^2 in the parameter space (P^{tot} , $P_T^{\%}$) for the three different Ekman numbers considered here. The dashed lines mark the tentative boundaries between dipolar

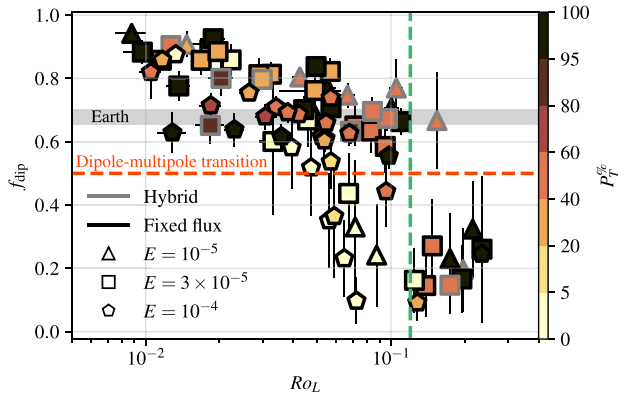


Figure 10. The dipolar fraction f_{dip} as a function of the local Rossby number Ro_L . Geophysical range of f_{dip} based on the COV-OBS.x1 model by Gillet *et al.* (2015). Black markers correspond to simulations with $P_T^{\%} = 100\%$, while white ones correspond to simulations with $P_T^{\%} = 0\%$. The horizontal dashed line marks the limit between dipolar and multipolar dynamos adopted in this study (see Section 2.5 for details). The vertical dashed line marks the expected limit between dipolar and multipolar dynamos according to Christensen & Aubert (2006). Vertical and horizontal black segments attached to each symbol represent one standard deviation about the time-averaged values.

and multipolar simulations in term of P^{tot} . The dipole–multipole transition is delayed to larger input power P^{tot} at lower Ekman numbers. Decreasing E indeed enables the exploration of a physical regime with lower Ro prone to sustain dipole-dominated dynamos (see Kutzner & Christensen 2002; Christensen & Aubert 2006). The input power required to obtain multipolar dynamos is multiplied by roughly 300 when decreasing E from 10^{-4} to 10^{-5} . For each Ekman number, the width of the dipolar window strongly depends on $P_T^{\%}$ since the actual input power needed to reach the transition is an order of magnitude lower for pure chemical convection than for pure thermal convection. Simulations with $P_T^{\%} = 40\%$ are found to behave similarly to purely thermal convection. We further observe that Earth-like dynamos can be obtained for any partitioning of power injection with the best agreement obtained close to the dipole–multipole transition. This is a consequence of the way we have sampled the parameter space, mainly adopting one single Pm value for each Ekman number. Magnetic Reynolds numbers $Rm \sim \mathcal{O}(1000)$ conducive to yield Earth-like fields are then attained at strong convective forcings. Adopting larger Pm values at more moderate chemical and thermal Rayleigh numbers could hence produce Earth-like fields further away from the dipole–multipole transition (see Christensen *et al.* 2010). Additional diagnostics are hence required to better understand why the dipole–multipole transition depends so strongly on the nature of the convective forcing.

3.4 Breakdown of the dipole

The physical reasons which cause the breakdown of the dipole in numerical models remain poorly known. Several previous studies suggest that the dipole may collapse when inertia reaches a sizeable contribution in the force balance (see Sreenivasan & Jones 2006; Christensen & Aubert 2006).

Christensen & Aubert (2006) introduced the local Rossby number Ro_L as a proxy of the ratio between inertia and Coriolis force and found no dipole-dominated dynamos for $Ro_L > 0.12$ (see Christensen 2010). Fig. 10 shows f_{dip} as a function of Ro_L for the 79 simulations computed in this study. The vertical line marks the threshold

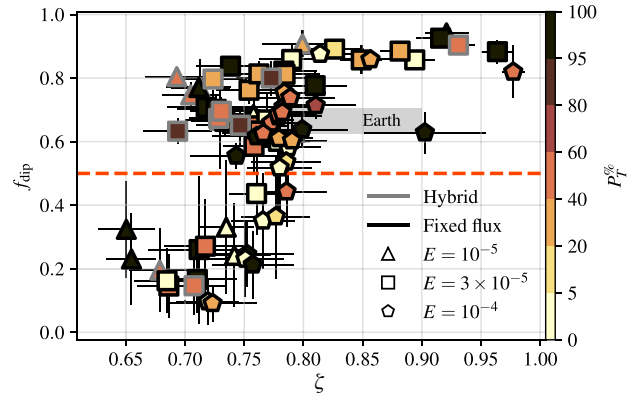


Figure 11. The dipolar fraction f_{dip} as a function of the relative fraction of equatorially symmetric kinetic energy ζ for the 79 simulations computed in this study. Geophysical range of f_{dip} based on the COV-OBS.x1 model by Gillet *et al.* (2015). Geophysical estimates of ζ are based on the study of Aubert (2014). Black markers correspond to simulations with $P_T^{\%} = 100\%$, while white ones correspond to simulations with $P_T^{\%} = 0\%$. The horizontal dashed line marks the limit between dipolar and multipolar dynamos adopted in this study (see Section 2.5 for details). Vertical and horizontal black segments attached to each symbol represent one standard deviation about the time-averaged values.

value of $Ro_L = 0.12$ put forward by Christensen & Aubert (2006), while the horizontal line corresponds to $f_{\text{dip}} = 0.5$, the boundary between dipolar and multipolar dynamos adopted in this study. To single out the effect of partitioning the input power between chemical and thermal forcings, the symbols have been colour coded according to $P_T^{\%}$. Each subset of models with comparable $P_T^{\%}$ exhibits the same decrease of f_{dip} with Ro_L as reported by Christensen & Aubert (2006). However, the dipole–multipole transition occurs at lower Ro_L when $P_T^{\%}$ decreases. For $P_T^{\%} \geq 40\%$, the transition happens close to $Ro_L = 0.12$ while it happens around $Ro_L = 0.05$ for $P_T^{\%} = 0\%$. In addition, the dynamo models with $P_T^{\%} \geq 40\%$ are clearly separated in two groups of simulations with either $f_{\text{dip}} \geq 0.5$ or $f_{\text{dip}} < 0.3$, while the dipole–multipole transition is much more gradual for pure chemical forcing. Ro_L hence fails to capture the transition between dipolar and multipolar dynamos, independently of the transport properties of the convecting fluid.

Following Christensen & Aubert (2006), Garcia *et al.* (2017) also envision that the increasing role of inertia would be responsible for the dipole breakdown. They however define another parameter to characterize it. They suggest that the transition is related to a change in the equatorial symmetry properties of the convective flow. To quantify it, they introduce the ratio ζ previously defined in eq. (16). Fig. 11 shows f_{dip} as a function of ζ . Geophysical estimates for ζ are based on the study of Aubert (2014). The decrease of the relative equatorial symmetry ζ goes along with a gradual weakening of the axisymmetric dipolar field. Below $\zeta = 0.7$, no dipolar dynamos are obtained while conversely the models with $\zeta \geq 0.85$ are all dipolar. However, this parameter has little predictive power to separate the dipolar solutions from the multipolar ones over the intermediate range $0.7 \leq \zeta \leq 0.85$.

Another way to examine the dipole–multipole transition resorts to looking at the force balance governing the outer core flow dynamics (see Soderlund *et al.* 2012, 2015). To do so, we analyse force balance spectra following Aubert *et al.* (2017) and Schwaiger *et al.* (2019). Each force entering the Navier–Stokes eq. (3) is hence decomposed into spherical harmonic contributions. The spatial root mean square

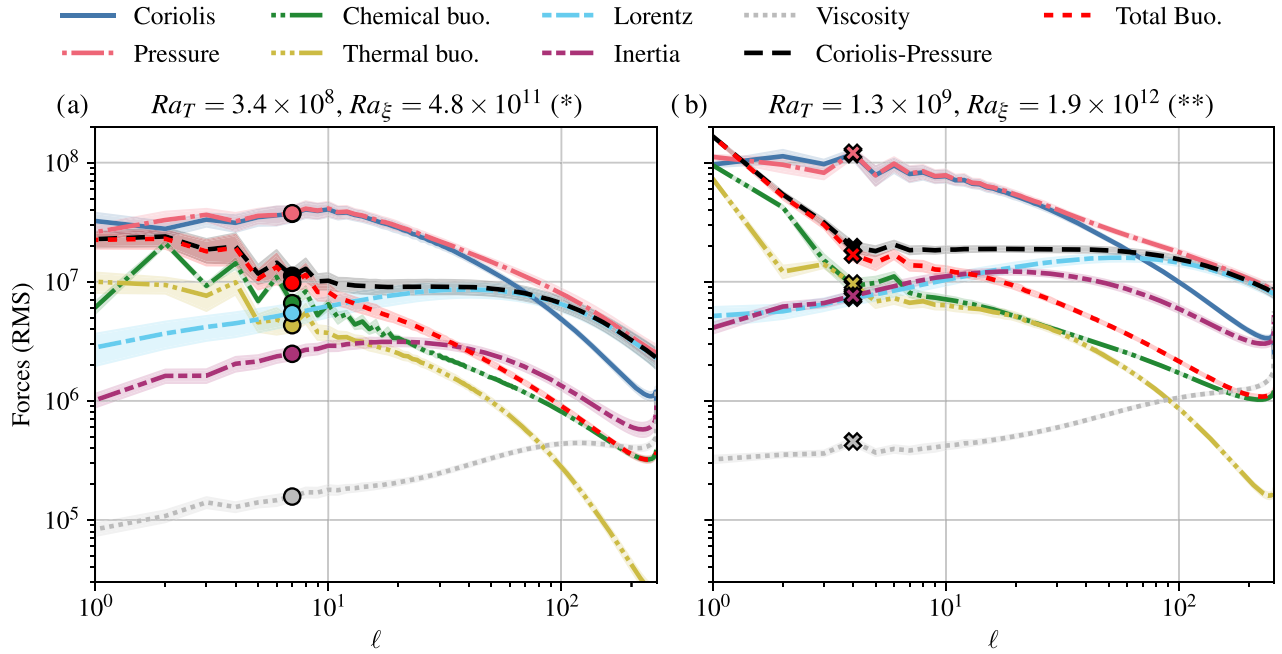


Figure 12. Force balance spectra as a function of the spherical harmonic degree ℓ for a dipolar (a) and a multipolar (b) simulations with $E = 10^{-5}$ and $P_T^{\%} \approx 46\%$. Thick lines correspond to the time average of each force, while the shaded regions represent one standard deviation about mean. The abscissa of the markers corresponds to the dominant lengthscale $\bar{\ell}$ for each simulation. A circle corresponds to a dipolar simulation while a cross corresponds to a multipolar one. Both simulations are referenced as simulations (*) and (**) in Table A1.

F_{RMS} of a vector \mathbf{F} reads

$$F_{\text{RMS}}(t) = \sqrt{\langle \mathbf{F}^2(\mathbf{r}, t) \rangle_{V_{o\delta}}}, \quad (23)$$

where δ represents the thickness of the viscous boundary layer and $V_{o\delta}$ the outer core volume that excludes those boundary layers. By using the decomposition in spherical harmonics, the above expression can be rearranged as

$$F_{\text{RMS}}^2(t) = \frac{1}{V_{o\delta}} \sum_{\ell=0}^{\ell_{\max}} \int_{r_i+\delta}^{r_o-\delta} \sum_{m=-\ell}^{\ell} |F_{\ell m}(r, t)|^2 r^2 dr,$$

We define the time-averaged spectrum F^ℓ as a function of the harmonic degree ℓ for the force \mathbf{F} by the relation

$$F^\ell = \sqrt{\frac{1}{V_{o\delta}} \int_{r_i+\delta}^{r_o-\delta} \sum_{m=-\ell}^{\ell} |F_{\ell m}(r, t)|^2 r^2 dr}. \quad (24)$$

Fig. 12 shows the time-averaged force balance spectra for one dipolar and one multipolar dynamo with $E = 10^{-5}$ and $P_T^{\%} \simeq 46\%$. For both panels, the spherical harmonic at which the poloidal kinetic energy peaks $\bar{\ell}$ is indicated by filled markers.

The left panel corresponds to the force balance of the reference case (*) which is in excellent agreement with the geomagnetic field in terms of its low χ^2 value (recall Section 3.2). Its spectra feature a dominant quasi-geostrophic balance between Coriolis and pressure forces up to $\ell \approx 60$ accompanied by a magnetostrophic balance at smaller scales. The difference between pressure and Coriolis forces, forming the so-called ageostrophic Coriolis force (long dashed line), is then balanced by the two buoyancy sources (short dashed line) at large scales and by Lorentz force (irregular dashed line) at small scales. This forms the quasi-geostrophic Magneto–Archimedean–Coriolis balance (QG-MAC) devised by Davidson (2013) and expected to control the outer core fluid dynamics (see Roberts & King

2013). This hierarchy of forces is similar to the one observed in geodynamo models that use a codensity approach (e.g. Aubert *et al.* 2017; Schwaiger *et al.* 2019). The breakdown of buoyancy sources reveals a dominant contribution of chemical forcings which grows at small scales. The QG-MAC balance is perturbed by a sizeable inertia, which reaches almost a third of the amplitude of Lorentz force below $\ell \approx 20$, while viscous effects are deferred to more than one order of magnitude below. Because of the strong convective forcing, the force separation is hence not as pronounced as in the exemplary dipolar cases by (Schwaiger *et al.* 2019, their fig. 2).

By increasing the input power by a factor 4 while keeping $P_T^{\%}$ constant, we obtain a numerical model (**) (see Table A1 and Fig. 4c) where dynamo action yields a multipolar field. As compared to the dipole-dominated solution, the amplitude of each contribution is hence shifted to higher values. Most notable changes concern the prominent contribution of the chemical buoyancy for the degree $\ell = 1$ and the ratio of inertia to Lorentz force. The former comes from a pronounced equatorial asymmetry of the chemical fluctuations. The development of strong equatorially asymmetric convective motions has been observed by Landeau & Aubert (2011) and Dietrich & Wicht (2013) with a codensity approach and flux boundary conditions. Below $\ell \approx 20$, inertia reaches a comparable amplitude to Lorentz force, while the smaller scales are still controlled by magnetic effects. This differs from the multipolar dynamo model described by Schwaiger *et al.* (2019), where inertia was significantly larger than Lorentz force at all scales forming the so-called quasi-geostrophic Coriolis–Inertia–Archimedean balance (e.g. Gillet & Jones 2006). Here the situation differs likely because of the larger Pm , which enables a stronger magnetic field (see Menu *et al.* 2020). At the dominant lengthscale $\bar{\ell}$, the ratio F_i^ℓ/F_L^ℓ is around 1 for the multipolar model, while it is less than 0.5 for the dipolar one. To examine whether the dipole–multipole transition is controlled by the ratio of inertia over Lorentz forces, we hence focus on the

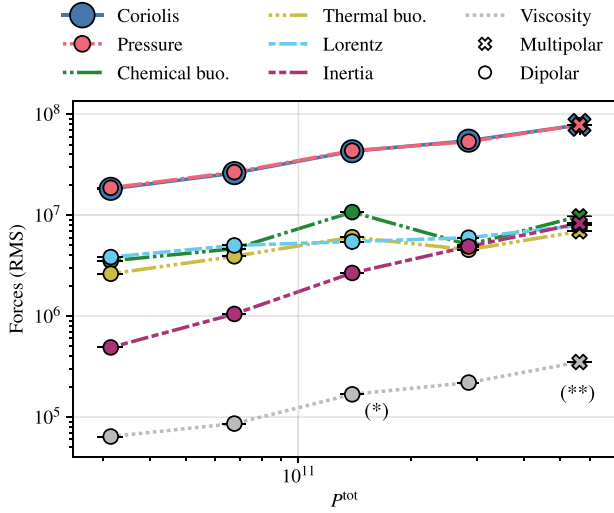


Figure 13. Time-averaged force balance spectra at the dominant lengthscale $\hat{\ell}$ as a function of the total buoyancy power P^{tot} for numerical models with $E = 10^{-5}$ and $30\% \leq P_T^{\%} \leq 60\%$. The dynamo models (*) and (**) correspond to simulations referenced in Table A1. The horizontal and vertical segments attached to each symbol correspond to one standard deviation about the time-averaged values.

force balance at the dominant lengthscale $\hat{\ell}$, in contrast to previous studies, which analysed ratio of integrated forces (Soderlund *et al.* 2012, 2015; Yadav *et al.* 2016).

Fig. 13 shows the time-averaged force balance at $\hat{\ell}$ for the simulations with $E = 10^{-5}$ and $30\% \leq P_T^{\%} \leq 60\%$. The dynamics at $\hat{\ell}$ is primarily controlled by the geostrophic balance between the Coriolis force and the pressure gradient. The other contributions

grow differently with P^{tot} : viscosity and inertia increase continuously while Lorentz force at $\hat{\ell}$ hardly increases beyond $P^{\text{tot}} \approx 3 \times 10^{10}$. The dipole–multipole transition occurs when inertia reaches a comparable amplitude to Lorentz force at $\hat{\ell}$ (crosses).

The relevance of this force ratio for sustaining the dipolar field has already been put forward by Menu *et al.* (2020), using models with a purely thermal forcing and $Pr = 1$. By considering turbulent simulations with large Pm , they show that strong Lorentz forces at large scale prevent the collapse of the dipole by inertia. As a result, they report dipole-dominated simulations with Ro_L which exceeds the limit of 0.12 proposed by Christensen & Aubert (2006). Here, we quantify the contribution of inertia at the dominant convective lengthscale by dividing the amplitude of inertia $F_i^{\hat{\ell}}$ by the amplitude of Coriolis $F_C^{\hat{\ell}}$ and Lorentz $F_L^{\hat{\ell}}$ forces.

Fig. 14(a) shows our simulations in the parameter space defined by the amplitude ratios $(F_i^{\hat{\ell}}/F_L^{\hat{\ell}}, F_i^{\hat{\ell}}/F_C^{\hat{\ell}})$. Each simulation is characterized by the proportion of thermal convection $P_T^{\%}$ and the nature of its thermal boundary conditions. Increasing the input power of the dynamo leads to a growth of inertia, such that the strongly driven cases all lie in the upper right quadrant of Fig. 14(a). The transition from dipolar to multipolar dynamos occurs sharply when $F_i^{\hat{\ell}}/F_L^{\hat{\ell}}$ exceeds 0.5 over a broad range of $F_i^{\hat{\ell}}/F_C^{\hat{\ell}}$ ranging from 0.03 to 0.08. This indicates that the transition is much more sensitive to the ratio of inertia over Lorentz force than to the ratio of inertia over Coriolis force. The transition for purely chemical simulations (white symbols) is reached at lower values of $F_i^{\hat{\ell}}/F_C^{\hat{\ell}}$ and is more continuous than for the thermal ones (black symbols). This confirms the trend already observed in Fig. 10, where f_{dip} shows a much more gradual decrease with Ro_L when $P_T^{\%} = 0\%$.

Fig. 14(b) shows f_{dip} as a function of $F_i^{\hat{\ell}}/F_L^{\hat{\ell}}$. In contrast to the previous criteria, the ratio $F_i^{\hat{\ell}}/F_L^{\hat{\ell}}$ successfully captures the transition between dipole-dominated and multipolar dynamos which happens when $F_i^{\hat{\ell}}/F_L^{\hat{\ell}} \simeq 0.5$, independently of the buoyancy power

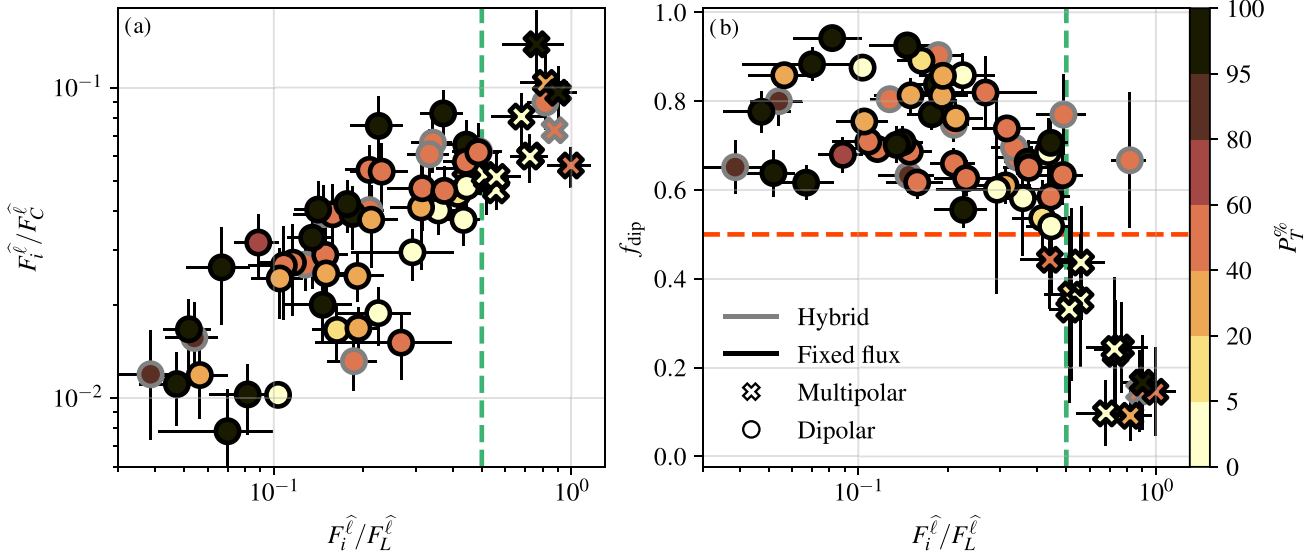


Figure 14. Ratio of inertia to Coriolis force at the dominant lengthscale $F_i^{\hat{\ell}}/F_C^{\hat{\ell}}$ (left-hand panel) and the dipolar fraction f_{dip} (right-hand panel) as a function of the ratio of inertia to the Lorentz force at the dominant lengthscale $F_i^{\hat{\ell}}/F_L^{\hat{\ell}}$. Black markers correspond to simulations with $P_T^{\%} = 100\%$, while white markers correspond to simulations with $P_T^{\%} = 0\%$. Horizontal dashed line marks the limit between dipolar and multipolar dynamo according to Section 2.5. Vertical dashed line marks the limit between dipolar and multipolar dynamo in term of $F_i^{\hat{\ell}}/F_L^{\hat{\ell}}$ ratio. Vertical and horizontal black segments attached to the symbol correspond to one standard deviation about the time-averaged values.

fraction. The simulation, which singles out in the upper right quadrant of Fig. 14(b), is an exception to this criterion. This numerical model corresponds to $P_T^{\%} \approx 47\%$ with $Ra_T = 6.8 \times 10^{10}$, $Ra_{\xi} = 9.6 \times 10^{11}$ with hybrid boundary conditions. Although it features $F_i^{\hat{r}}/F_L^{\hat{r}} > 0.5$, its magnetic field is on time-average dominated by an axisymmetric dipole ($f_{\text{dip}} = 0.69$). This dynamo however strongly varies with time with several drops of the dipolar component below $f_{\text{dip}} = 0.5$ (see Fig. A1 in the appendix). Although the numerical model has been integrated for more than two magnetic diffusion times, the stability of the dipole cannot be granted for certain.

4 SUMMARY AND DISCUSSION

Convection in the liquid outer core of the Earth is thought to be driven by density perturbations from both thermal and chemical origins. In the vast majority of geodynamo models, the difference between the two buoyancy sources is simply ignored. In planetary interiors with huge Reynolds numbers, diffusion processes associated with molecular diffusivities could indeed possibly be superseded by turbulent eddy diffusion (see Braginsky & Roberts 1995). This hypothesis forms the backbone of the so-called ‘codensity’ approach which assumes that both thermal and compositional diffusivities are effectively equal. This approach suppresses some dynamic regimes intrinsic to double-diffusive convection (Radko 2013).

The main goal of this study is to examine the impact of double-diffusive convection on the magnetic field generation when both thermal and compositional gradients are destabilizing (the so-called top-heavy regime, see Takahashi 2014). To do so we have computed 79 global dynamo models, varying the fraction between thermal and compositional buoyancy sources $P_T^{\%}$, the Ekman number E and the vigor of the convective forcing using a Prandtl number $Pr = 0.3$ and a Schmidt number $Sc = 3$. We have explored the influence of the thermal boundary conditions by considering two sets of boundary conditions for temperature and composition.

Using a generalized eigenvalue solver, we have first investigated the onset of thermosolutal convection. In agreement with previous studies (Busse 2002; Net *et al.* 2012; Trümper *et al.* 2012; Silva *et al.* 2019), we have shown that the incorporation of a destabilizing compositional gradient actually facilitates the onset of convection as compared to the single diffusive configurations by reducing the critical thermal Rayleigh number. The critical onset mode in the top-heavy regime of rotating double-diffusive convection is otherwise similar to classical thermal Rossby waves obtained in purely thermal convection (Busse 1970).

To quantify the Earth-likeness of the magnetic fields produced by the non-linear dynamo models, we have used the rating parameters introduced by Christensen *et al.* (2010). Using geodynamo models with a codensity approach, Christensen *et al.* (2010) suggested that the Earth-like dynamo models are located in a wedge-like shape in the 2-D parameter space constructed from the ratio of three typical timescales, namely the rotation rate, the turnover time and the magnetic diffusion time. Here, we have shown that the physical parameters at which the best morphological agreement with the geomagnetic field is attained strongly depend on the ratio of thermal and compositional input power. In particular, we obtain 6 purely compositional multipolar dynamo models that lie within the wedge region of Earth-like dynamos (recall Fig. 8a). This questions the relevance of the regime boundaries proposed by Christensen *et al.* (2010).

We have then used our set of double-diffusive dynamos to examine the transition between dipolar and multipolar dynamos. We have

assessed the robustness of several criteria controlling this transition that had been proposed in previous studies. Sreenivasan & Jones (2006) suggested that the dipole breakdown results from an increasing role played by inertia at strong convective forcings. Christensen & Aubert (2006) then introduced the local Rossby number Ro_L as a proxy of the ratio of inertial to Coriolis forces. They suggested that $Ro_L \approx 0.12$ marks the boundary between dipole-dominated and multipolar dynamos over a broad range of control parameters. Our numerical dynamo models with $P_T^{\%} \geq 40\%$ follow a similar behaviour, while the transition between dipolar and multipolar dynamos occurs at lower Ro_L (≈ 0.05) when chemical forcing prevails. A breakdown of the dipole for dynamo models with $Ro_L < 0.1$ was already reported by Garcia *et al.* (2017) using $Pr > 1$ under the codensity hypothesis (their Fig. 1).

Using non-magnetic numerical models, Garcia *et al.* (2017) further argued that the breakdown of the dipolar field is correlated with a change in the equatorial symmetry properties of the convective flow. They introduced the relative proportion of kinetic energy contained in the equatorially symmetric convective flow, ζ , and suggested that multipolar dynamos would be associated with a lower value of this quantity. However, our numerical data set shows that multipolar and dipolar dynamos coexist over a broad range of ζ (0.70–0.85, recall Fig. 11), indicating that this ratio has little predictive power in separating dipolar from multipolar simulations.

While neither Ro_L nor ζ provide a satisfactory measure to characterize the dipole–multipole transition, the analysis of the force balance governing the dynamo models has been found to be a more promising avenue to decipher the physical processes at stake (Soderlund *et al.* 2012, 2015). By considering a spectral decomposition of the different forces (e.g. Aubert *et al.* 2017; Schwaiger *et al.* 2019), we have shown that the transition between dipolar and multipolar dynamos goes along with an increase of inertia at large scales. The analysis of the force ratio at the dominant scale of convection has revealed that the dipole–multipole transition is much more sensitive to the ratio of inertia to Lorentz force than to the ratio of inertia to Coriolis force. The transition from dipolar to multipolar dynamos robustly happens when the ratio of inertial to magnetic forces at the dominant lengthscale of convection exceeds 0.5, independently of $P_T^{\%}$ and the Ekman number. This confirms the results by Menu *et al.* (2020) who argued that a strong Lorentz force prevents the demise of the axial dipole, delaying its breakdown beyond $Ro_L \approx 0.12$ (their figs 3 and 4).

Providing a geophysical estimate of the ratio of inertial to magnetic forces at the dominant scale of convection in the Earth’s core is not an easy task. Recent work by Schwaiger *et al.* (2021) suggests that the dominant scale of convection should be that at which the Lorentz force and the buoyancy force, both second-order actors in the force balance, equilibrate. Extrapolation of this finding to Earth’s core yields a scale of approximately 200 km, that corresponds to spherical harmonic degree 40. This is far beyond what can be constrained through the analysis of the geomagnetic secular variation. Estimating the strength of both Lorentz and inertial forces at that scale is hence out of reach.

We can however try to approximate the ratio of these two forces by a simpler proxy, namely the ratio of the total kinetic energy E_k to total magnetic energy E_m . To examine the validity of this approximation, Fig. 15 shows f_{dip} as a function of the ratio E_k/E_m for our numerical simulations complemented with the codensity simulations of Christensen (2010) that have $Pr \neq 1$. We observe that the dipolar fraction f_{dip} exhibits a variation similar to that shown in Fig. 14(b) for the actual force ratio. The transition between dipolar and multipolar dynamos is hence adequately captured by the ratio

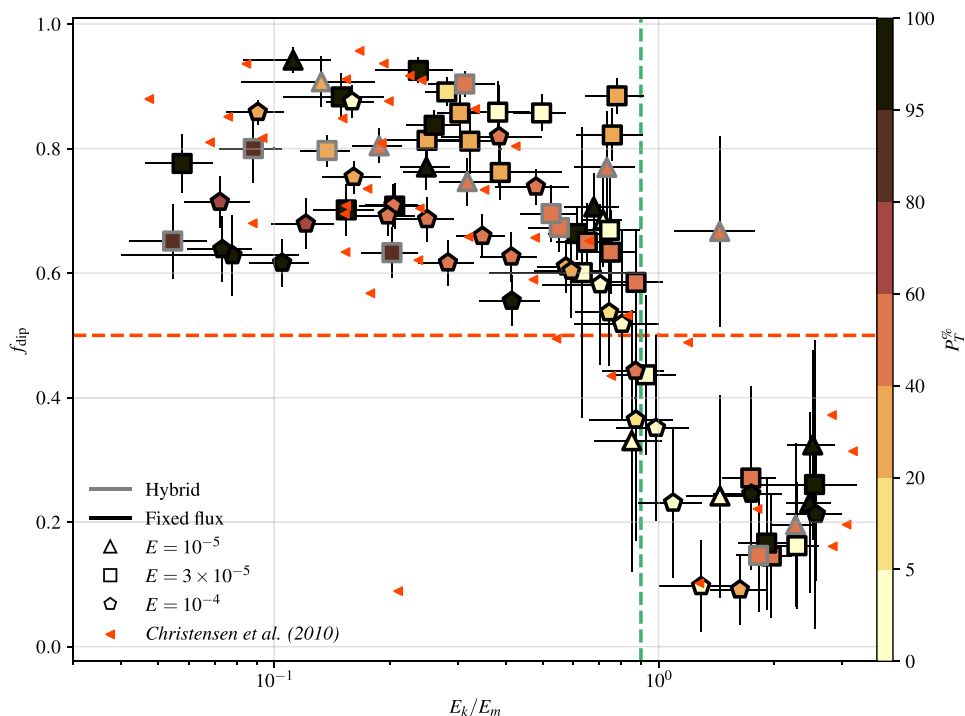


Figure 15. Dipolarity parameter f_{dip} as a function of the kinetic to magnetic energy ratio E_k/E_m . The triangles correspond to those simulations by Christensen (2010) with $Pr \neq 1$. The horizontal dashed line marks the $f_{\text{dip}} = 0.5$ limit between dipolar and multipolar dynamos. The vertical dashed line corresponds to $E_k/E_m = 0.9$. Vertical and horizontal black segments attached to the symbols correspond to one standard deviation about the time-averaged values for f_{dip} and E_k/E_m , respectively.

E_k/E_m (Kutzner & Christensen 2002). All but one of the numerical dynamos of our data set become multipolar for $E_k/E_m > 0.9$, independently of E , P_T^ω , and the type of thermal boundary conditions prescribed. Using the physical properties from Table 1 leads to the following estimate for the Earth's core

$$\frac{E_k}{E_m} = \mu_0 \rho_o \frac{w_{\text{rms}}^2}{B_{\text{rms}}^2} \approx 10^{-4} - 10^{-3} \ll \mathcal{O}(1).$$

Christensen (2010) and Wicht & Tilgner (2010) argued that convection in the Earth's core should operate in the vicinity of the transition between dipolar and multipolar dynamos in order to explain the reversals of the geomagnetic field. This statement, however, postulates that reversals and the dipole breakdown are governed by the same physical mechanism. The smallness of E_k/E_m for Earth's core indicates that it should operate far from the dipole–multipole transition, contrary to the numerical evidence accumulated up to now. The palaeomagnetic record indicates that during a reversal or an excursion, the intensity of the field is remarkably low, which suggests that the strength of the geomagnetic field could decrease by about an order of magnitude. This state of affairs admittedly brings the ratio E_k/E_m closer to unity, yet without reaching it. So it seems that the occurrence of geomagnetic reversals is not directly related to an increase of the relative amplitude of inertia. Other mechanisms proposed to explain geomagnetic reversals rely on the interaction of a limited number of magnetic modes, whose nonlinear evolution is further subject to random fluctuations (e.g. Schmitt *et al.* 2001; P  tr  lis *et al.* 2009). In this useful conceptual framework, the large-scale dynamics of Earth's magnetic field is governed by the induction equation alone. The origin of the fluctuations that can potentially lead to a reversal of polarity is not explicated and

it remains to be found, but evidence from mean fields models by Stefani *et al.* (2006) suggests that the likelihood of reversals increases with the magnetic Reynolds number. In practice, these fluctuations could very well occur in the vicinity of the convective length scale, and have either an hydrodynamic, or a magnetic, or an hydro-magnetic origin, depending on the process driving the instability. Shedding light on the origin of these fluctuations constitutes an interesting avenue for future numerical investigations of geomagnetic reversals.

ACKNOWLEDGEMENTS

We would like to thank Ulrich Christensen and Julien Aubert for sharing their data. Numerical computations were performed at SCAPAD, IPGP and using HPC resources from GENCI-CINES and TGCC-Irene KNL (Grant 2020-A0070410095). Those computations required roughly 3.3 millions single core hours on Intel Haswell CPUs. This amounts for 33 MWh, or equivalently to a bit more than 3 tons of carbon dioxide emissions. We thank Gabriel Hautreux, from GENCI-CINES, for providing us with a direct measure of the power consumption of MagIC. All the figures have been generated using matplotlib (Hunter 2007) and paraview (<https://www.paraview.org>). The colourbar used in this study were designed by Thyng *et al.* (2016) and Cramer (2018, 2019).

DATA AVAILABILITY

The data underlying this article will be shared on reasonable request to the corresponding author.

REFERENCES

- Anufriev, A.P., Jones, C.A. & Soward, A.M., 2005. The Boussinesq and anelastic liquid approximations for convection in the Earth's core, *Phys. Earth planet. Inter.*, **152**, 163–190.
- Ascher, U.M., Ruuth, S.J. & Spiteri, R.J., 1997. Implicit-explicit Runge-Kutta methods for time-dependent partial differential equations, *Appl. Numer. Math.*, **25**(2–3), 151–167.
- Aubert, J., 2014. Earth's core internal dynamics 1840–2010 imaged by inverse geodynamo modelling, *Geophys. J. Int.*, **197**(3), 1321–1334.
- Aubert, J., Finlay, C.C. & Fournier, A., 2013. Bottom-up control of geomagnetic secular variation by the Earth's inner core, *Nature*, **502**, 219–223.
- Aubert, J., Gastine, T. & Fournier, A., 2017. Spherical convective dynamos in the rapidly rotating asymptotic regime, *J. Fluid Mech.*, **813**, 558–593.
- Badro, J., Fiquet, G., Guyot, F., Gregoryanz, E., Occelli, F., Antonangeli, D. & Astuto, M., 2007. Effect of light elements on the sound velocities in solid iron: Implications for the composition of Earth's core, *Earth planet. Sci. Lett.*, **254**, 233–238.
- Boscario, S., Pareschi, L. & Russo, G., 2013. Implicit-explicit Runge-Kutta Schemes for Hyperbolic Systems and Kinetic Equations in the Diffusion Limit, *SIAM J. Sci. Comput.*, **35**(1), A22–A51.
- Bouffard, M., 2017. *Double-diffusive thermochemical convection in the liquid layers of planetary interiors: a first numerical exploration with a particle-in-cell method*, Theses, Université de Lyon.
- Boyd, J.P., 2001. *Chebyshev and Fourier Spectral Methods*, 2nd revised edn, Courier Corporation.
- Braginsky, S.I. & Roberts, P.H., 1995. Equations governing convection in earth's core and the geodynamo, *Geophys. Astrophys. Fluid Dyn.*, **79**, 1–97.
- Breuer, M., Manglik, A., Wicht, J., Trümper, T., Harder, H. & Hansen, U., 2010. Thermochemically driven convection in a rotating spherical shell, *Geophys. J. Int.*, **183**, 150–162.
- Buffett, B., 2015. Core-mantle interactions, in *Treatise on Geophysics*, 2nd edn, Vol. **8**, pp. 345–358, ed. Schubert, G., Elsevier.
- Busse, F.H., 1970. Thermal instabilities in rapidly rotating systems, *J. Fluid Mech.*, **44**(3), 441–460.
- Busse, F.H., 2002. Is low Rayleigh number convection possible in the Earth's core?, *Geophys. Res. Lett.*, **29**(7), 9.
- Butcher, J.C., 1964. On Runge-Kutta processes of high order, *J. Aust. Math. Soc.*, **4**(2), 179–194.
- Christensen, U., Olson, P. & Glatzmaier, G.A., 1999. Numerical modelling of the geodynamo: a systematic parameter study, *Geophys. J. Int.*, **138**(2), 393–409.
- Christensen, U. *et al.*, 2001. A numerical dynamo benchmark, *Phys. Earth planet. Inter.*, **128**(1–4), 25–34.
- Christensen, U.R., 2010. Dynamo scaling laws and applications to the planets, *Space Sci. Rev.*, **152**(1), 565–590.
- Christensen, U.R. & Aubert, J., 2006. Scaling properties of convection-driven dynamos in rotating spherical shells and application to planetary magnetic fields, *Geophys. J. Int.*, **166**, 97–114.
- Christensen, U.R. & Wicht, J., 2015. Numerical dynamo simulations, in *Treatise on Geophysics*, 2nd edn, Vol. **8**, pp. 245–282, ed. Schubert, G., Elsevier.
- Christensen, U.R., Aubert, J. & Hulot, G., 2010. Conditions for Earth-like geodynamo models, *Earth planet. Sci. Lett.*, **296**, 487–496.
- Cramer, F., 2018. Geodynamic diagnostics, scientific visualisation and StagLab 3.0, *Geosci. Model Dev.*, **11**(6), 2541–2562.
- Cramer, F., 2019. Scientific Colour Maps, Zenodo.
- Davidson, P., 2013. Scaling laws for planetary dynamos, *Geophys. J. Int.*, **195**(1), 67–74.
- Dietrich, W. & Wicht, J., 2013. A hemispherical dynamo model: Implications for the Martian crustal magnetization, *Phys. Earth planet. Inter.*, **217**, 10–21.
- Dormy, E., Soward, A.M., Jones, C.A., Jault, D. & Cardin, P., 2004. The onset of thermal convection in rotating spherical shells, *J. Fluid Mech.*, **501**, 43–70.
- Dziewonski, A.M. & Anderson, D.L., 1981. Preliminary reference earth model, *Phys. Earth planet. Inter.*, **25**, 297–356.
- Finlay, C.C. & Amit, H., 2011. On flow magnitude and field-flow alignment at Earth's core surface: Core flow magnitude and field-flow alignment, *Geophys. J. Int.*, **186**(1), 175–192.
- Finlay, C.C. *et al.*, 2010. International geomagnetic reference field: the eleventh generation, *Geophys. J. Int.*, **183**(3), 1216–1230.
- Garcia, F., Oruba, L. & Dormy, E., 2017. Equatorial symmetry breaking and the loss of dipolarity in rapidly rotating dynamos, *Geophys. Astrophys. Fluid Dyn.*, **111**(5), 380–393.
- Gastine, T., 2019. Pizza: An open-source pseudo-spectral code for spherical quasi-geostrophic convection, *Geophys. J. Int.*, **217**(3), 1558–1576.
- Gastine, T., Wicht, J. & Aurnou, J.M., 2015. Turbulent Rayleigh-Bénard convection in spherical shells, *J. Fluid Mech.*, **778**, 721–764.
- Gastine, T., Wicht, J. & Aubert, J., 2016. Scaling regimes in spherical shell rotating convection, *J. Fluid Mech.*, **808**, 690–732.
- Gillet, N. & Jones, C.A., 2006. The quasi-geostrophic model for rapidly rotating spherical convection outside the tangent cylinder, *J. Fluid Mech.*, **554**(-1), 343.
- Gillet, N., Jault, D., Canet, E. & Fournier, A., 2010. Fast torsional waves and strong magnetic field within the Earth's core, *Nature*, **465**(7294), 74–77.
- Gillet, N., Barrois, O. & Finlay, C.C., 2015. Stochastic forecasting of the geomagnetic field from the COV-OBS. x1 geomagnetic field model, and candidate models for IGRF-12, *Earth, Planets and Space*, **67**(1), 71.
- Glatzmaier, G.A., 1984. Numerical simulations of stellar convective dynamos. I - the model and method, *J. Comput. Phys.*, **55**, 461–484.
- Glatzmaier, G.A. & Roberts, P.H., 1995. A three-dimensional convective dynamo solution with rotating and finitely conducting inner core and mantle, *Phys. Earth planet. Inter.*, **91**, 63–75.
- Glatzmaier, G.A. & Roberts, P.H., 1996. An anelastic evolutionary geodynamo simulation driven by compositional and thermal convection, *Phys. D Nonlin. Phenom.*, **97**, 81–94.
- Goluskin, D., 2016. *Internally Heated Convection and Rayleigh-Bénard Convection*, Springer Briefs in Applied Sciences and Technology, Springer.
- Hirose, K., Labrosse, S. & Hernlund, J., 2013. Composition and state of the core, *Ann. Rev. Earth planet. Sci.*, **41**, 657–691.
- Hollerbach, R., 2000. A spectral solution of the magneto-convection equations in spherical geometry, *Int. J. Numer. Methods Fluids*, **32**(7), 773–797.
- Hunter, J.D., 2007. Matplotlib: a 2D graphics environment, *Comput. Sci. Eng.*, **9**(3), 90–95.
- Jackson, A., Jonkers, A.R.T. & Walker, M.R., 2000. Four centuries of geomagnetic secular variation from historical records, *Phil. Trans. R. Soc. Lond., A*, **358**(1768), 957–990.
- Jameson, A., Schmidt, W. & Turkel, E., 1981. Numerical solution of the Euler equations by finite volume methods using Runge Kutta time stepping schemes, in *Proceedings of the 14th Fluid and Plasma Dynamics Conference*, American Institute of Aeronautics and Astronautics, Palo Alto, CA, USA.
- Johnston, H. & Doering, C.R., 2009. Comparison of turbulent thermal convection between conditions of constant temperature and constant flux, *Phys. Rev. Lett.*, **102**(6), 064501.
- Kaplan, E.J., Schaeffer, N., Vidal, J. & Cardin, P., 2017. Subcritical thermal convection of liquid metals in a rapidly rotating sphere, *Phys. Rev. Lett.*, **119**(9), 094501.
- King, E.M., Stellmach, S. & Aurnou, J.M., 2012. Heat transfer by rapidly rotating Rayleigh-Bénard convection, *J. Fluid Mech.*, **691**, 568–582.
- Konôpková, Z., McWilliams, S.R., Gómez-Pérez, N. & Goncharov, A.F., 2016. Direct measurements of thermal conductivity in solid iron at planetary core conditions, *Nature*, **534**(7605), 99–101.
- Korte, M., Genevey, A., Constable, C.G., Frank, U. & Schnepf, E., 2005. Continuous geomagnetic field models for the past 7 millennia: 1. A new global data compilation, *Geochem. Geophys. Geosyst.*, **6**(2), doi:10.1029/2004GC000800.
- Kosloff, D. & Tal-Ezer, H., 1993. A modified Chebyshev pseudospectral method with an O(N-1) time step restriction, *J. Comput. Phys.*, **104**(2), 457–469.
- Kutzner, C. & Christensen, U., 2002. From stable dipolar towards reversing numerical dynamos, *Phys. Earth planet. Inter.*, **131**(1), 29–45.

- Labrosse, S., 2003. Thermal and magnetic evolution of the Earth's core, *Phys. Earth planet. Inter.*, **140**(1–3), 127–143.
- Labrosse, S., 2015. Thermal evolution of the core with a high thermal conductivity, *Phys. Earth planet. Inter.*, **247**, 36–55.
- Landeau, M. & Aubert, J., 2011. Equatorially asymmetric convection inducing a hemispherical magnetic field in rotating spheres and implications for the past martian dynamo, *Phys. Earth planet. Inter.*, **185**(3–4), 61–73.
- Li, Y., Fruehan, R.J., Lucas, J.A. & Belton, G.R., 2000. The chemical diffusivity of oxygen in liquid iron oxide and a calcium ferrite, *Metall. Mater. Trans., B*, **31**(5), 1059–1068.
- Lister, J.R. & Buffett, B.A., 1995. The strength and efficiency of thermal and compositional convection in the geodynamo, *Phys. Earth planet. Inter.*, **91**, 17–30.
- Loper, D.E. & Roberts, P.H., 1981. A study of conditions at the inner core boundary of the earth, *Phys. Earth planet. Inter.*, **24**(4), 302–307.
- Manglik, A., Wicht, J. & Christensen, U.R., 2010. A dynamo model with double diffusive convection for Mercury's core, *Earth planet. Sci. Lett.*, **289**, 619–628.
- Marti, P., Calkins, M.A. & Julien, K., 2016. A computationally efficient spectral method for modeling core dynamics, *Geochem. Geophys. Geosyst.*, **17**(8), 3031–3053.
- Mather, J.F. & Simitev, R.D., 2021. Regimes of thermo-compositional convection and related dynamos in rotating spherical shells, *Geophys. Astrophys. Fluid Dyn.*, **115**(1), 61–84.
- Matsui, H. *et al.*, 2016. Performance benchmarks for a next generation numerical dynamo model, *Geochem. Geophys. Geosyst.*, **17**(5), 1586–1607.
- Menu, M.D., Petitdemange, L. & Galtier, S., 2020. Magnetic effects on fields morphologies and reversals in geodynamo simulations, *Phys. Earth planet. Inter.*, doi:10.1016/j.pepi.2020.106542.
- Moll, R., Garaud, P. & Stellmach, S., 2016. A new model for mixing by double-diffusive convection (semi-convection). III. Thermal and compositional transport through non-layered ODDC, *Astrophys. J.*, **823**, 33.
- Monville, R., Vidal, J., Cébron, D. & Schaeffer, N., 2019. Rotating convection in stably-stratified planetary cores, *Geophys. J. Int.*, **219**(Suppl. 1), S195–S218.
- Net, M., García, F. & Sánchez, J., 2012. Numerical study of the onset of thermosolutal convection in rotating spherical shells, *Phys. Fluids*, **24**(6), 064101.
- Olson, P. & Christensen, U.R., 2006. Dipole moment scaling for convection-driven planetary dynamos, *Earth planet. Sci. Lett.*, **250**(3–4), 561–571.
- Olson, P., Christensen, U.R. & Glatzmaier, G.A., 1999. Numerical modelling of the geodynamo: mechanism of field generation and equilibration, *J. geophys. Res.*, **104**(B5), 10383–10404.
- Oruba, L. & Dormy, E., 2014. Transition between viscous dipolar and inertial multipolar dynamos, *Geophys. Res. Lett.*, **41**(20), 7115–7120.
- Parker, E.N., 1955. Hydromagnetic dynamo models, *Astrophys. J.*, **122**, 293.
- Pétrétil, F., Fauve, S., Dormy, E. & Valet, J.-P., 2009. Simple mechanism for reversals of earth's magnetic field, *Phys. Rev. Lett.*, **102**(14), 144503.
- Pozzo, M., Davies, C., Gubbins, D. & Alfè, D., 2013. Transport properties for liquid silicon-oxygen-iron mixtures at Earth's core conditions, *Phys. Rev. B*, **87**, doi:10.1103/PhysRevB.87.014110.
- Press, W.H., Flannery, B.P., Teukolsky, S.A. & Vetterling, W.T., 1992. *Numerical Recipes in Fortran: The Art of Scientific Computing*, 2nd edn, Vol. 1 of Fortran Numerical Recipes, Cambridge Univ. Press.
- Quidelleur, X. & Courtillot, V., 1996. On low-degree spherical harmonic models of paleosecular variation, *Phys. Earth planet. Inter.*, **95**(1–2), 55–77.
- Radko, T., 2013. *Double-Diffusive Convection*, Cambridge Univ. Press.
- Roberts, P.H. & King, E.M., 2013. On the genesis of the Earth's magnetism, *Rep. Prog. Phys.*, **76**, 096801, doi:10.1088/0034-4885/76/9/096801.
- Ruddick, B., 1983. A practical indicator of the stability of the water column to double-diffusive activity, *Deep Sea Res., A. Oceanogr. Res. Papers*, **30**(10), 1105–1107.
- Schaeffer, N., 2013. Efficient spherical harmonic transforms aimed at pseudo-spectral numerical simulations, *Geochem. Geophys. Geosyst.*, **14**(3), 751–758.
- Schaeffer, N., 2016. Effective scaling for the onset of thermal convection in rotating planetary cores, *Figshare*, https://figshare.com/articles/figure/Effective_scaling_for_the_onset_of_thermal_convection_in_rotating_planetary_cores/4231376..
- Schaeffer, N., Jault, D., Nataf, H.C. & Fournier, A., 2017. Turbulent geodynamo simulations: a leap towards Earth's core, *Geophys. J. Int.*, **211**(1), 1–29.
- Schmitt, D., Ossendrijver, M.A.J.H. & Hoyng, P., 2001. Magnetic field reversals and secular variation in a bistable geodynamo model, *Phys. Earth planet. Inter.*, **125**(1–4), 119–124.
- Schwaiger, T., Gastine, T. & Aubert, J., 2019. Force balance in numerical geodynamo simulations: a systematic study, *Geophys. J. Int.*, **219**(Suppl. 1), S101–S114.
- Schwaiger, T., Gastine, T. & Aubert, J., 2021. Relating force balances and flow length scales in geodynamo simulations, *Geophys. J. Int.*, **224**, 1890–1904.
- Silva, L., Mather, J.F. & Simitev, R.D., 2019. The onset of thermo-compositional convection in rotating spherical shells, *Geophys. Astrophys. Fluid Dyn.*, **113**(4), 377–404.
- Simitev, R.D., 2011. Double-diffusive convection in a rotating cylindrical annulus with conical caps, *Phys. Earth planet. Inter.*, **186**, 183–190.
- Soderlund, K.M., King, E.M. & Aurnou, J.M., 2012. The influence of magnetic fields in planetary dynamo models, *Earth planet. Sci. Lett.*, **333–334**, 9–20.
- Soderlund, K.M., Sheyko, A., King, E.M. & Aurnou, J.M., 2015. The competition between Lorentz and Coriolis forces in planetary dynamos, *Prog. Earth planet. Sci.*, **2**(1), 24.
- Spiegel, E.A., 1972. Convection in stars: II. Special effects, *Ann. Rev. Astron. Astrophys.*, **10**, 261.
- Sreenivasan, B. & Jones, C.A., 2006. The role of inertia in the evolution of spherical dynamos, *Geophys. J. Int.*, **164**(2), 467–476.
- Sreenivasan, B. & Jones, C.A., 2011. Helicity generation and subcritical behaviour in rapidly rotating dynamos, *J. Fluid Mech.*, **688**, 5–30.
- Stefani, F., Gerbeth, G., Günther, U. & Xu, M., 2006. Why dynamos are prone to reversals, *Earth planet. Sci. Lett.*, **243**(3–4), 828–840.
- Takahashi, F., 2014. Double diffusive convection in the Earth's core and the morphology of the geomagnetic field, *Phys. Earth planet. Inter.*, **226**, 83–87.
- Takahashi, F., Shimizu, H. & Tsunakawa, H., 2019. Mercury's anomalous magnetic field caused by a symmetry-breaking self-regulating dynamo, *Nat. Commun.*, **10**, 208.
- Thyng, K., Greene, C., Hetland, R., Zimmerle, H. & DiMarco, S., 2016. True colors of oceanography: guidelines for effective and accurate colormap selection, *Oceanography*, **29**(3), 9–13.
- Tilgner, A., 1999. Spectral methods for the simulation of incompressible flows in spherical shells, *Int. J. Numer. Methods Fluids*, **30**(6), 713–724.
- Trümper, T., Breuer, M. & Hansen, U., 2012. Numerical study on double-diffusive convection in the Earth's core, *Phys. Earth planet. Inter.*, **194**, 55–63.
- Valet, J.-P. & Fournier, A., 2016. Deciphering records of geomagnetic reversals, *Rev. Geophys.*, **54**(2), 410–446.
- Vidal, J. & Schaeffer, N., 2015. Quasi-geostrophic modes in the Earth's fluid core with an outer stably stratified layer, *Geophys. J. Int.*, **202**(3), 2182–2193.
- Wicht, J., 2002. Inner-core conductivity in numerical dynamo simulations, *Phys. Earth planet. Inter.*, **132**(4), 281–302.
- Wicht, J. & Sanchez, S., 2019. Advances in geodynamo modelling, *Geophys. Astrophys. Fluid Dyn.*, **113**(1–2), 2–50.
- Wicht, J. & Tilgner, A., 2010. Theory and modeling of planetary dynamos, *Space Sci. Rev.*, **152**(1), 501–542.
- Yadav, R.K., Gastine, T. & Christensen, U.R., 2013. Scaling laws in spherical shell dynamos with free-slip boundaries, *Icarus*, **225**(1), 185–193.
- Yadav, R.K., Gastine, T., Christensen, U.R., Wolk, S.J. & Poppenhaeger, K., 2016. Approaching a realistic force balance in geodynamo simulations, *PNAS*, **113**(43), 12065–12070.
- Zhang, Y. *et al.*, 2020. Reconciliation of experiments and theory on transport properties of iron and the geodynamo, *Phys. Rev. Lett.*, **125**(7), 078501.

APPENDIX A: TIME SCHEME

We provide in this appendix the matrices \mathbf{a}^I and \mathbf{a}^E and the vectors \mathbf{b}^I , \mathbf{b}^E , \mathbf{c}^E and \mathbf{c}^I of the two IMEX Runge–Kutta schemes that we resorted to for this study. These vectors and matrices can conveniently be represented using Butcher tables (Butcher 1964).

BPR353: (Boscarino *et al.* 2013)
Implicit component

$$\frac{\mathbf{c}^I | \mathbf{A}^I}{\mathbf{b}^I} = \begin{array}{c|ccc} 0 & 0 & & \\ 1 & 1/2 & 1/2 & \\ \hline 2/3 & 5/18 & -1/9 & 1/2 \\ 1 & 1/2 & 0 & 0 & 1/2 \\ \hline 1 & 1/4 & 0 & 3/4 & -1/2 & 1/2 \\ \hline & 1/4 & 0 & 3/4 & -1/2 & 1/2 \end{array}$$

Explicit component

$$\frac{\mathbf{c}^E | \mathbf{A}^E}{\mathbf{b}^E} = \begin{array}{c|ccc} 0 & 0 & & \\ 1 & 1 & 0 & \\ \hline 2/3 & 4/9 & 2/9 & 0 \\ 1 & 1/4 & 0 & 3/4 & 0 \\ \hline 1 & 1/4 & 0 & 3/4 & 0 & 0 \\ \hline & 1/4 & 0 & 3/4 & 0 & 0 \end{array}$$

PC2: (Jameson *et al.* 1981)
Implicit component

$$\frac{\mathbf{c}^I | \mathbf{A}^I}{\mathbf{b}^I} = \begin{array}{c|ccc} 0 & 0 & & \\ 1 & 1/2 & 1/2 & \\ \hline 1 & 1/2 & 0 & 1/2 \\ 1 & 1/2 & 0 & 0 & 1/2 \\ \hline & 1/2 & 0 & 0 & 1/2 \end{array}$$

Explicit component

$$\frac{\mathbf{c}^E | \mathbf{A}^E}{\mathbf{b}^E} = \begin{array}{c|ccc} 0 & 0 & & \\ 1 & 1 & 0 & \\ \hline 1 & 1/2 & 1/2 & 0 \\ 1 & 1/2 & 0 & 1/2 & 0 \\ \hline & 1/2 & 0 & 1/2 & 0 \end{array}$$

APPENDIX B: NUMERICAL SIMULATIONS

Table A1. Control parameters and simulation diagnostics for the 79 numerical simulations computed for this study. Simulations computed using the finite difference method in radius are marked with a superscript f (the others were computed using the Chebyshev collocation method in radius). Simulations with hybrid boundary conditions are marked by an H in the first column. Simulations are sorted by growing Ekman number and then by growing magnetic Reynolds number. The averaging and running times t_{avg} and t_{run} are expressed in units of magnetic diffusion time τ_η .

	Ra_T ($\times 10^8$)	Ra_ξ ($\times 10^9$)	(N_r, ℓ_{max})	Pm	α	t_{scheme}	t_{avg}	t_{run}	Rm	Ro_L ($\times 10^{-2}$)	Λ	f_{ohm}	χ^2	ζ	f_{dip}	$P_T^{\%}$	Nu	Sh
$E = 1 \times 10^{-5}, Pr = 0.3, Sc = 3$																		
H	0.1	10	(97, 133)	1.0	0.935	BPR353	1.80	1.80	176	1.5	2.4	0.66	20.1	0.80	0.91	32	1.8	10.6
	3.1	0	(97, 170)	1.0	0.935	BPR353	2.79	3.09	196	0.9	3.4	0.79	12.6	0.92	0.94	100	2.0	1.0
	0	100	(193, 213)	1.0	0.975	BPR353	0.29	0.29	444	4.9	2.7	0.51	3.4	0.76	0.69	0	1.0	26.6
H	0.8	120	(257, 256)	1.0	0.990	BPR353	0.20	0.37	514	4.3	14.1	0.74	1.8	0.69	0.80	40	4.5	28.1
	0	270	(320, 256) ^f	1.0	None	BPR353	0.47	0.95	685	7.2	5.5	0.54	7.9	0.73	0.33	0	1.0	36.2
	0	400	(380, 256) ^f	1.0	None	BPR353	0.16	0.20	880	8.7	5.4	0.49	14.5	0.74	0.24	0	1.0	41.0
	46	0	(109, 170)	1.0	0.940	BPR353	0.38	0.90	763	5.5	23.5	0.75	2.4	0.71	0.77	100	7.3	1.0
H	1.7	240	(321, 256)	1.0	0.992	BPR353	0.17	0.28	760	6.7	18.2	0.70	2.2	0.70	0.75	44	6.1	35.3
H	3.4	480	(384, 341) ^f	0.5	None	BPR353	0.46	0.67	580	10.5	9.2	0.65	1.5	0.71	0.77	46	8.0	44.8 (*)
	100	0	(129, 213)	1.0	0.932	BPR353	0.26	1.29	1213	10	21.7	0.67	0.8	0.72	0.71	100	10.5	1.0
H	6.8	960	(380, 256) ^f	0.5	None	BPR353	1.54	1.88	843	15.3	10.3	0.60	1.9	0.73	0.69	47	11.0	55.3 (*)
	300	0	(129, 256)	0.5	0.962	BPR353	0.30	1.22	1235	17.4	12.4	0.58	19.2	0.65	0.23	100	16.7	1.0
H	13	1900	(408, 256) ^f	0.5	None	PC2	0.16	0.24	1252	19.7	13.8	0.57	21.2	0.68	0.20	47	14.2	68.2 (**)
	600	0	(129, 256)	0.5	0.962	BPR353	0.22	0.43	1640	21.6	21.4	0.61	11.6	0.65	0.32	100	20.9	1.0

Table A1. Continued

Ra_T ($\times 10^8$)	Ra_ξ ($\times 10^9$)	(N_r, ℓ_{max})	Pm	α	t_{scheme}	t_{avg}	t_{run}	Rm	Ro_L ($\times 10^{-2}$)	Λ	f_{ohm}	χ^2	ζ	f_{dip}	$P_T^{\%}$	Nu	Sh	
$E = 3 \times 10^{-5}, Pr = 0.3, Sc = 3$																		
	0	0.5	(49, 106)	2.0	0.779	CNAB2	1.37	1.55	113	1.2	0.4	0.30	52.3	0.89	0.86	0	1.0	4.0
H	0.015	0.5	(49, 133)	2.0	0.779	CNAB2	1.95	2.33	154	1.3	1.1	0.47	24.0	0.93	0.90	44	1.3	4.6
H	0.1	1.1	(49, 133)	1.0	0.779	CNAB2	2.15	4.39	98	2	0.4	0.31	36.5	0.88	0.88	21	1.4	6.3
H	0.1	1.1	(129, 213)	2.0	0.960	BPR353	0.15	3.11	178	1.7	1.6	0.48	10.7	0.85	0.86	22	1.4	6.4
	0.1	1.4	(129, 170)	2.0	0.960	BPR353	0.35	1.79	193	1.8	2.0	0.51	13.4	0.83	0.89	19	1.5	7.2
	0	2	(65, 133)	2.0	0.848	CNAB2	1.81	2.26	204	2.2	1.6	0.43	8.5	0.79	0.86	0	1.0	8.2
	0.5	0	(49, 133)	2.0	0.779	CNAB2	1.62	1.71	255	1	6.6	0.68	8.9	0.96	0.88	100	1.7	1.0
	0	4	(97, 133)	2.0	0.975	CNAB2	1.24	1.42	288	3.3	2.0	0.38	2.3	0.78	0.60	0	1.0	11.2
H	0.2	4	(97, 133)	2.0	0.930	CNAB2	1.04	1.32	307	2.9	4.4	0.54	3.4	0.78	0.81	20	2.0	11.5
	1	0	(49, 106)	1.0	0.779	CNAB2	5.96	6.41	180	1.9	4.1	0.69	10.8	0.92	0.93	100	2.1	1.0
	1	0	(49, 106)	2.0	0.864	CNAB2	0.79	1.18	281	1.4	20.6	0.81	3.4	0.81	0.78	100	2.4	1.0
	0	8	(97, 133)	2.0	0.975	CNAB2	1.91	5.45	385	4.6	3	0.41	2.6	0.77	0.67	0	1.0	14.8
	0.1	1.1	(97, 133)	1.0	0.935	CNAB2	1.30	1.77	164	2.0	9.2	0.79	5.0	0.77	0.80	86	2.2	9.2
H	0.5	5.5	(129, 170)	2.0	0.960	CNAB2	1.21	1.21	373	3.3	8.4	0.62	2.3	0.76	0.81	35	2.4	13.4
	0.1	1.1	(97, 133)	2.0	0.935	CNAB2	1.61	1.89	317	1.8	27.8	0.79	5.9	0.75	0.65	87	2.3	8.9
	0.05	5.5	(65, 133)	2.0	0.864	CNAB2	1.63	1.81	342	3	12.8	0.69	2.2	0.72	0.80	39	2.2	12.9
	1	11	(97, 133)	1.0	0.935	CNAB2	1.10	1.30	297	5.7	3.5	0.51	4.0	0.78	0.82	39	3.1	17.9
	1	11	(145, 170)	2.0	0.960	CNAB2	1.08	1.23	541	4.9	11.4	0.59	1.5	0.75	0.76	39	3.2	17.4
	0	20	(97, 133)	2.0	0.975	CNAB2	1.04	1.06	581	6.7	5.5	0.43	5.6	0.76	0.44	0	1.0	20.0
	3.7	0	(49, 133)	1.0	0.779	CNAB2	1.31	1.41	328	5	12.4	0.71	2.8	0.74	0.84	100	4.0	1.0
	3.7	0	(81, 133)	2.0	0.900	CNAB2	0.88	1.02	613	4.4	36.7	0.72	3.7	0.73	0.70	100	4.0	1.0
	1.7	20	(145, 170)	2.0	0.970	CNAB2	0.83	1.08	738	7.1	12.5	0.54	1.7	0.76	0.65	40	4.0	21.3
	5	0	(97, 133)	2.0	0.864	CNAB2	0.89	1.06	726	5.7	38.6	0.69	2.8	0.72	0.71	100	4.6	1.0
	2.3	27	(129, 133)	2.0	0.960	CNAB2	1.07	1.07	857	8.3	14.7	0.53	1.7	0.76	0.63	41	4.6	23.3
	0.2	30	(109, 256)	2.0	0.948	BPR353	1.02	1.10	837	8.4	20	0.57	1.5	0.73	0.70	40	4.0	23.0
H	0.4	8	(97, 170)	2.0	0.962	BPR353	0.95	1.09	755	6.9	42.4	0.68	4.2	0.69	0.63	84	4.2	17.3
	3	35	(129, 170)	2.0	0.962	CNAB2	1.13	1.13	976	9.5	16.4	0.52	1.8	0.76	0.59	42	5.2	25.2
H	0.3	35	(129, 213)	2.0	0.962	BPR353	0.43	0.51	949	9.7	24.5	0.57	1.6	0.73	0.67	48	4.6	24.2
	0	100	(193, 213)	2.0	0.970	BPR353	0.13	0.18	1378	12.5	12.4	0.40	26.0	0.68	0.16	0	1.0	31.5
	12	0	(129, 170)	2.0	0.960	CNAB2	0.94	1.02	1237	11	37.5	0.59	2.5	0.73	0.66	100	6.8	1.0
	7	70	(193, 170)	2.0	0.983	CNAB2	0.87	1.22	1579	13.9	19	0.44	27.2	0.69	0.15	47	7.2	31.1
	9	100	(193, 256)	2.0	0.983	PC2	0.10	0.30	1765	14.8	27	0.49	12.2	0.72	0.27	45	8.2	33.1
H	0.9	100	(193, 213)	2.0	0.983	PC2	0.12	0.16	1790	17.4	26.5	0.47	26.3	0.71	0.15	51	7.3	32.6
	40	0	(97, 213)	2.0	0.960	CNAB2	0.34	0.38	2521	19.5	50	0.50	22.2	0.71	0.17	100	11.0	1.0
	68	0	(129, 170)	1.0	0.960	BPR353	0.59	0.59	1671	23.5	33	0.53	7.4	0.71	0.26	100	13.0	1.0
$E = 1 \times 10^{-4}, Pr = 0.3, Sc = 3$																		
	0.013	0.045	(49, 85)	5.0	None	CNAB2	1.09	1.78	175	1.1	1.6	0.32	10.1	0.98	0.82	40	1.2	2.8
	0	0.1	(65, 106)	5.0	None	CNAB2	1.17	1.31	161	1.3	3.2	0.47	4.9	0.81	0.88	0	1.0	3.8
	0.02	0.09	(49, 85)	5.0	None	CNAB2	2.54	7.73	180	1.2	7.2	0.62	4.3	0.86	0.86	36	1.3	4.0
	0.1	0	(65, 106)	5.0	None	CNAB2	1.86	2.16	363	1.3	34.7	0.67	11.9	0.90	0.63	100	1.7	1.0
	0	0.5	(49, 85)	5.0	None	CNAB2	1.65	1.99	378	3.9	4	0.32	1.8	0.79	0.58	0	1.0	7.6
	0.047	0.33	(65, 85)	5.0	None	BPR353	0.50	3.64	345	2.6	14.8	0.58	2.8	0.78	0.75	37	1.6	6.9
	0.08	0.19	(65, 106)	5.0	None	CNAB2	1.10	1.18	334	1.8	31	0.69	3.8	0.81	0.71	67	1.7	6.0
	0	0.7	(49, 85)	5.0	None	CNAB2	2.02	2.43	438	4.7	4.8	0.31	2.8	0.78	0.52	0	1.0	8.6
	0.07	0.5	(97, 106)	5.0	None	BPR353	0.35	1.70	438	3.4	18.9	0.56	3.0	0.78	0.71	40	1.8	8.1
	0	1	(65, 106)	5.0	None	CNAB2	1.06	1.33	522	5.6	5.5	0.31	8.1	0.77	0.35	0	1.0	9.9
	0.14	0.34	(65, 106)	5.0	None	CNAB2	1.08	1.09	482	3.1	38.6	0.64	3.8	0.78	0.68	70	2.0	7.7
	0.19	0	(65, 106)	5.0	None	CNAB2	1.14	1.36	469	2.3	60.1	0.69	5.0	0.80	0.64	100	2.0	1.0
	0.12	0.52	(81, 106)	5.0	None	BPR353	0.89	2.24	516	3.8	27.1	0.58	3.3	0.78	0.69	56	2.0	8.6
	0.027	1.1	(65, 106)	5.0	None	CNAB2	2.11	2.44	580	5.9	7.7	0.34	6.3	0.78	0.36	10	1.9	10.4
	0.027	1.1	(65, 106)	5.0	None	CNAB2	1.14	1.30	570	5.7	8.8	0.37	2.9	0.79	0.54	11	1.9	10.3
	0.1	0.69	(65, 106)	5.0	None	CNAB2	1.12	1.45	533	4.2	22.8	0.55	3.4	0.78	0.69	44	2.0	9.1
	0.049	1	(65, 106)	5.0	None	CNAB2	1.05	1.16	573	5.4	11.1	0.41	2.5	0.79	0.60	20	1.9	10.1
	0.049	1	(65, 133)	5.0	None	BPR353	0.13	1.38	566	5.4	11.2	0.42	2.2	0.78	0.61	20	1.9	10.1
	0	1.4	(65, 106)	5.0	None	CNAB2	1.32	1.61	615	6.5	7	0.31	16.6	0.75	0.23	0	1.0	11.0
	0.14	1	(65, 106)	3.0	None	BPR353	0.33	2.10	412	5.7	11.8	0.50	2.5	0.79	0.74	45	2.3	10.6
	0.14	1	(81, 106)	5.0	None	BPR353	0.37	1.72	655	5.5	24.7	0.51	3.3	0.77	0.66	46	2.3	10.5
	0.14	1	(81, 133)	7.0	0.909	BPR353	0.42	2.36	896	5.2	40.6	0.52	4.3	0.77	0.62	46	2.3	10.4
	0	2	(97, 170)	5.0	0.935	BPR353	0.88	2.98	750	7.2	8.7	0.32	39.4	0.72	0.10	0	1.0	12.4
	0.3	0	(61, 170)	5.0	None	CNAB2	0.16	1.24	616	3.6	72.6	0.66	4.7	0.76	0.62	100	2.4	1.0
	0.21	1.5	(81, 133)	5.0	0.909	BPR353	0.32	2.74	813	6.8	32	0.51	3.9	0.77	0.63	49	2.7	12.0
	0.3	3	(97, 170)	5.0	0.935	BPR353	0.28	2.13	1144	9.6	30.2	0.44	6.8	0.79	0.44	43	3.3	14.6
	0.9	0	(81, 170)	5.0	0.909	BPR353	0.34	2.08	1244	9.8	74.9	0.54	6.9	0.74	0.56	100	3.8	1.0
	0.4	6	(97, 213)	5.0	0.935	BPR353	0.29	1.85	1576	12.8	30.6	0.38	42.7	0.72	0.09	35	4.0	17.4
	5	0	(73, 213)	5.0	0.889	BPR353	0.33	1.49	3363	23.5	130	0.39	17.7	0.75	0.25	100	7.4	1.0
	20	0	(129, 170)	5.0	0.960	CNAB2	0.12	0.39	6160	45.1	297	0.36	21.9					

APPENDIX C: SIMULATION ^x

In this appendix we provide in Fig. A1 the detailed time evolution of the dipolar fraction f_{dip} and of the magnetic to kinetic energy ratio E_m/E_k of the anomalous simulation that appears for instance in the top-right quadrant of Figs 14(b) and 15. This simulation is marked with a (x) in Table A1.

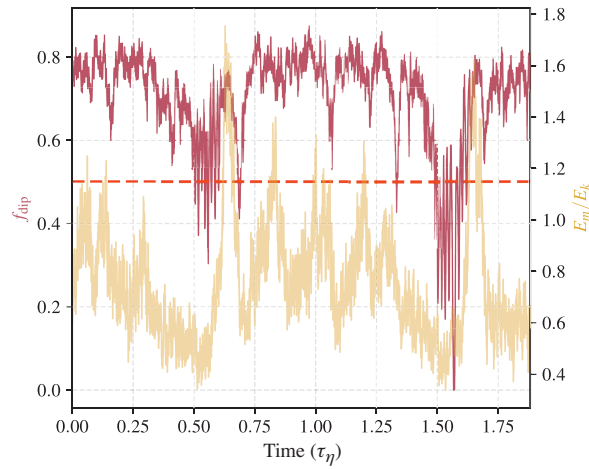


Figure A1. Time evolution of the dipolar fraction f_{dip} and of the magnetic to kinetic energy ratio E_m/E_k for the simulation (x) of Table A1. The horizontal dashed line corresponds to the boundary between dipole-dominated and multipolar dynamos ($f_{\text{dip}} = 0.5$). Time is scaled by the magnetic diffusion time.